Nonlinear Optics for Frequency-Doubling in Nanosatellite Laser Communication

by

James R. Clark

S.B. Aerospace Engineering, Massachusetts Institute of Technology
(2014)

Submitted to the Department of Aeronautics and Astronautics
in partial fulfillment of the requirements for the degree of

Master of Science in Aerospace Engineering

at the

MASSACHUSETTS INSTITUTE OF TECHNOLOGY

June 2016

Author ..... Signature redacted
Department of Aeronautics and Astronautics
May 19, 2016

Certified by ..... Signature redacted
Kerri Cahoy
Assistant Professor
Thesis Supervisor

Accepted by ..... Signature redacted
Paulo Lozano
Chairman, Department Committee on Graduate Theses

Nonlinear Optics for Frequency-Doubling in Nanosatellite Laser Communication

by

James R. Clark

Submitted to the Department of Aeronautics and Astronautics
on May 19, 2016, in partial fulfillment of the
requirements for the degree of
Master of Science in Aerospace Engineering

Abstract

In this work, we assess the utility of nonlinear optics for frequency-doubling to enable free space optical (FSO) communication links to take advantage of the ability to switch between two wavelengths using one transmit module. Our analysis shows that incorporating frequency-doubling with nonlinear optics into existing communication system designs can improve the link margin of FSO crosslinks by 3-4 dB, taking advantage of more favorable propagation and detector properties for the crosslink wavelength (775 nm) compared with the downlink wavelength (1550 nm). Using a frequency-doubler (65 g) allows the transmitter to use Commercial Off The Shelf (COTS) laser communication hardware at 1550 nm, without having to carry a second seed laser, modulator, and EDFA (200 g). This improvement is largely driven by the reduction in beamwidth that comes with the higher frequency, and is not substantially greater than the improvement that comes with using the same narrower beamwidth at 1550 nm, although SHG would allow a diffraction-limited system to use different beamwidths for beacon acquisition and communication without any moving parts. For links at extreme ranges, where linear-mode APDs are insufficient and photon-counting Geiger-mode APDs are required, frequency-doubling can provide up to 10 dB of channel capacity improvement.

Additionally, frequency-doubling shows promise as a means to allow CubeSats and nano/microsatellites to use their communications lasers to also serve as satellite guidestars, and frequency-differencing may be employed to allow communication lasers to generate longer infrared wavelengths suitable for atmospheric spectroscopy.

Thesis Supervisor: Kerri Cahoy
Title: Assistant Professor

Acknowledgments

The author wishes to acknowledge Kerri Cahoy and Bill Farr for their advice and mentorship in this field, doctoral students Annie Marinan, Emily Clements, Kit Kennedy, and Ryan Kingsbury and MITLL personnel Dave Caplan, Dennis Burianek, Don Boroson, Jeff Mendenhall, Keith Doyle, and Mike Shatz for presentation feedback, and the 2016 Space Systems quals study group: Akshata Krishnamurthy, Ashley Carlton, Max Yates, Pronoy Biswas, and Weston Marlow.

Contents

List of Figures

List of Tables

List of Acronyms

APD Avalanche Photodiode

COTS Commercial Off The Shelf

DFG Difference Frequency Generation

FDOT Frequency-Doubling Optical Transmitter

FLARE Free-space Laser communication And Radiation Experiment

FSM Fine steering mirror

InGaAs Indium Gallium Arsenide

HPLD High-Power Laser Diode

LADEE Lunar Atmosphere and Dust Environment Explorer

LLCD Lunar Laser Communication Demonstration

KTP Potassium Titanyl Phosphate

MOPA Master Oscillator Power Amplifier

NFIRE Near Field InfraRed Experiment

NODE Nanosatellite Optical Downlink Experiment

OCSD Optical Communication and Sensor Demonstration

OPO Optical Parametric Oscillator

PPLN Periodically Poled Lithium Niobate

PPM pulse-position modulation

SHG Second Harmonic Generation

SNR Signal-to-noise ratio

List of variables

BER, bit error rate [n.d.]

C_{opt}, optical link capacity [bits/sec]

D_r, D_t: receiver and transmitter aperture diameters [m[1]]

d, laser beam divergence [mrad]

η, system efficiency [n.d.]

F_A, excess noise factor [n.d.]

F_n, R_{in}, noise factor and input resistance of next-stage amplifier [n.d., 50 Ω]

G_t, G_r, transmitter and receiver gain [n.d.]

h, orbital altitude [km]

I_l, I_{dg}, the photocurrent produced by incident photons (at unity gain, or $R_{APD}P_{rec}$) and dark current subjected to gain [A]

k_A, x, empirical material properties that F_A depends on [n.d.]

k_B, the Boltzmann constant [1.38×10^{-23} J/K]

L_r, L_t, L_{fs}, L_{atm}: losses from receiver optics, transmitter optics, free space, and the atmosphere [n.d.]

λ, wavelength [m].[2]

M_{APD}, APD gain [n.d.]

M_{PPM}, PPM order [n.d.]

m, apparent magnitude [n.d.]

[1] All length variables are measured in meters for all calculations, with the exception of Equation 5.1, but they may be expressed in more convenient units in discussion (e.g. km, nm).

[2] λ also stands for the expected electron count per gate in a Geiger-mode APD.

$\mu_{i,on}$, $\mu_{i,off}$, $\mu_{i,on,req}$, average photocurrent for on-pulse, off-pulse, and required [A]

P_t, P_r/P_{av}, P_{pk}, P_{off}, P_{req}: transmitted (optical) power, received (average) power, received peak power, received "off" power, and required power [W]

P_{elec}, P_{shg}, electrical power budget of the overall transmitter system and electrical power required to activate SHG [W]

η_{wp}, η_{shg}, wall-plug efficiency (i.e. electrical power to optical power) and SHG conversion efficiency (i.e. 1550 nm optical power to 775 nm optical power)

P, laser transmit power [mW]

Q, Q_{req}, quality factor and required quality factor

q, the elementary charge [1.602×10^{-19} C]

R, the link range [m]

R_{APD}, the responsivity of an APD at unity gain [Ω]

σ^2_{amp}, σ^2_{on}, σ^2_{off}, variance in photocurrent for the amplifier, on-pulse, and off-pulse [A^2]

T, APD temperature [K]

T_s, slot time [s]

For the Geiger-mode APD SNR calculations only:

λ_p, incident photons per gate

λ_d, dark count rate (charge carriers per gate)

PDE, photon detection efficiency (charge carriers generated per incident photon)

$\lambda = PDE\lambda_p + \lambda_d$, average number of charge carriers per gate[3]

[3]Not to be confused with wavelength, which is what λ represents in the rest of this research.

n_{gates}, number of gates [n.d.]

p_{aft}, probability of aftercounts [n.d.]

$P_1 = \frac{1-e^{-\lambda}}{1-p_{aft}e^{-\lambda}}$ [n.d.]

$P_0 = 1 - P_1 = \frac{e^{-\lambda(1-p_{aft})}}{1-p_{aft}e^{-\lambda}}$ [n.d.]

Chapter 1

Introduction

Free-space optical communication attracts interest due to its promise of higher data rates for similar size, weight, and power costs as radio systems. However, while satellite-to-ground optical communication has been tested from low Earth orbit and the Moon, intersatellite links are still an area of active research and development. This research lies at the intersection of three major fields: laser communication, nonlinear optics, and nanosatellites.

1.1 Laser communication

Interest in laser communication has grown in the commercial and exploration sectors. Terrestrial networks are underpinned by fiber-optic communication links, and the resulting availability of commodity lasers, modulators, amplifiers, and receivers has enabled the growth of free-space optical communication. The main reason for this is the increased data rate and less competitive frequency constraints that are available. At radio frequencies, the FCC requires users to submit applications for permission to use specific frequencies.[4] On the other hand, optical frequencies are regulated by the FAA, FDA, and Laser Clearinghouse; rather than allocating specific frequencies, their regulations focus on restricting output power to safe levels.[5]

Link budgets and channel capacity will be treated in more detail in section 2.1, but one key consideration is the received signal power.

$$P_r = P_t \left(\frac{\pi D_t D_r}{4R\lambda} \right)^2 \eta \tag{1.1}$$

As laid out in Equation 1.1[6], received power P_r depends on:

P_t, transmitted power [W],

D_r and D_t, receiver and transmitter aperture diameters [m[1]],

R, the link range [m],

η, system efficiency [n.d.], and

λ, the wavelength used [m].

In particular, moving from radio frequencies (with centimeter or millimeter wavelengths) to optical (with micrometer wavelengths) results in a narrower diffraction-limited beam divergence (the $\frac{1}{\lambda^2}$ dependency of the equation), which results in a factor of a million (or 60 dB) increase in received power. This can result in higher data rates, or be traded against other system factors to expand the design space. For example, it can allow a mission to use smaller, less powerful transmitters or receivers while maintaining the data rate achieved by a more massive radio system.

Other benefits of laser communication include improved security (as the narrower beams are more difficult to intercept or jam) and a less restrictive and competitive regulatory environment. Rather than obtaining frequency-specific licenses from the FCC, the use of visible spectrum in the United States is regulated by the FAA, FDA, and the DoD's Laser Clearinhouse. FAA regulations simply require that visible and invisible power densities remain below certain limits to be permitted.[5]

The narrower beam width does impose additional challenges for laser communication, requiring fine beam steering and tracking on the part of the transmitter and receiver. Large laser communication systems, such as the Lunar Laser Communication Demonstration[7], place their transmitters on a discrete gimbal, while smaller

[1]All length variables are measured in meters for all calculations, with the exception of Equation 5.1, but they may be expressed in more convenient units in discussion (e.g. km, nm).

systems such as NODE[8] use fine-steering mirrors. Free-space optical communication is also vulnerable to obscuration by weather, which has spurred interest in networks of satellites and ground stations which can be deployed in enough numbers to ensure availability. NODE and BridgeSat (San Mateo, CA)[9] are two examples of such development efforts.

1.1.1 Pulse-position modulation

NODE uses pulse-position modulation (PPM) to modulate information on the laser beam. In PPM of order M_{PPM}[2], transmission slots are bundled into groups of M_{PPM}, and a pulse is transmitted in one slot in each group. Each pulse then represents $\log_2 M_{PPM}$ bits. A simple case of PPM-4 is illustrated in Figure 1-1.

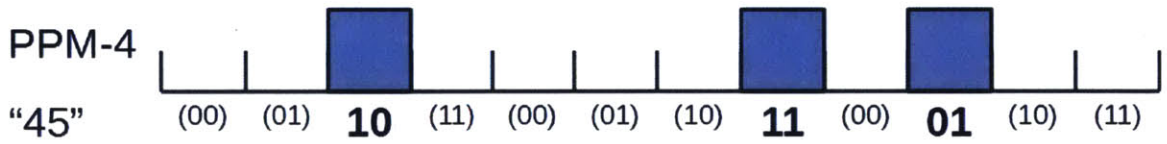

Figure 1-1: A simple illustration of PPM-4 encoding the number 45.

Because fewer pulses are made in comparison with e.g. phase-shift keying, the pulses can be made brighter while keeping the average power draw of the system the same. For example, in PPM-4, the laser is only active with a duty cycle of 25%, so each pulse can be four times as bright. This makes them easier to distinguish over long ranges or with smaller transmitters or receive apertures.

1.2 Nanosatellites

Nanosatellites are satellites with masses between 1 and 10 kilograms[10], a category which includes the popular CubeSat platform. CubeSats are a standardized form factor consisting of 10-centimeter-cubed units, currently arranged in 1U, 2U, 3U, and 6U assemblies. Because of their standard shapes and low masses, they can easily be

[2]PPM order is usually simply called M, as in "M-ary PPM", but M is also used to represent APD gain, so the terms are labeled in this research as M_{PPM} and M_{APD}.

accommodated on launch vehicles, and because of their small size and the growing availability of COTS parts, the cost of development is relatively low – on the order of $100k-10M[11]. These factors have led to a rapidly growing popularity of the CubeSat form factor; of the 208 satellites launched in 2014, 130 (or 63%) were CubeSats, which is an increase from 91 CubeSats launched in 2013 (out of 107 satellites total) [11].

The CubeSat concept was developed to reduce the cost of access to space for universities and research projects, although most of the CubeSats launched in recent years are commercial. MIT is pursuing several 3U and 6U CubeSat projects, including Nanosatellite Optical Downlink Experiment (NODE)[8], KitCube, and Free-space Laser communication And Radiation Experiment (FLARE)[2] in the field of optical communication.

The small size of nanosatellites brings new constraints to size, weight, and power. For example, KitCube, a 6U CubeSat, measures only $10 \times 20 \times 30$ cm, and its mass is limited to 14 kg. Its solar panels can only generate up to 50 watts[12]. OCSD, a 1.5U CubeSat, measures $10 \times 10 \times 15$ cm, and its mass budget is limited to 2 kg.

For nanosatellites seeking high-data-rate communication, all of these constraints motivate the consideration (and selection, in KitCube's case) of laser communication. As nanosatellites lack the volume or mass budgets to store large radio antennas, or the power budget to drive kilowatt-class amplifiers, the narrower beamwidths of optical systems become attractive.

1.3 Nonlinear optics

Nonlinear optics is a field of optics concerned with nonlinear interactions of light with matter. It is of interest here because it allows a system to have inputs at one frequency and outputs at another (or multiple others), which can be exploited if there are situations where different frequencies are more advantageous.

The propagation of electromagnetic waves is governed by Maxwell's equations:

$$\nabla \times \mathbf{E} = -\frac{\partial \mathbf{B}}{\partial t} \tag{1.2}$$

$$\nabla \times \mathbf{H} = \frac{\partial \mathbf{D}}{\partial t} + \mathbf{J} \tag{1.3}$$

$$\nabla \cdot \mathbf{D} = \rho \tag{1.4}$$

$$\nabla \cdot \mathbf{B} = 0 \tag{1.5}$$

For non-magnetic materials, $\mathbf{B}$ and $\mathbf{H}$ are proportional ($\mathbf{B} = \mu_0 \mathbf{H}$), but the displacement field $\mathbf{D}$ is connected to the electric field $\mathbf{E}$ by the polarization density field $\mathbf{P}$, which measures the dipole moments induced in the molecules of a material placed in an electric field.

$$\mathbf{D} = \epsilon_0 \mathbf{E} + \mathbf{P} \tag{1.6}$$

At electric field intensities below $\sim 10^5 - 10^8$ V/m [13], polarization is well-approximated by a linear relationship, characterized by susceptibility χ [14]:

$$\mathbf{P} = \epsilon_0 \chi \mathbf{E} \tag{1.7}$$

However, at higher intensities (as can be achieved with lasers) and in suitable materials, when the field is comparable in strength to inter-atomic forces, the linear approximation no longer holds, and it is necessary to consider higher-order nonlinear terms:

$$\mathbf{P} = \epsilon_0 \chi \mathbf{E} + \mathbf{P}_{NL} = \epsilon_0 \left(\chi \mathbf{E} + \chi^{(2)} \mathbf{E}^2 + \chi^{(3)} \mathbf{E}^3 + \cdots \right) \tag{1.8}$$

In general, each $\chi^{(n)}$ is an $(n+1)$-order tensor, and so the nonlinear polarization depends not only on field intensity and frequency, but also alignment of the input fields and crystal axes. However, the detailed mathematics of nonlinear optics are not in the scope of the current work; for the moment, it will suffice to deal with simple cases where all alignment has been arranged.

In linear systems, the output of a system is composed of exactly and only the frequencies of its input, with some gain or attenuation and phase delay encoded by a transfer function. This is not the case for nonlinear systems: it is possible for a signal at one frequency to modulate or generate an output signal at other frequencies. This property is the basis of many components used in optical communication, including lasers and optical amplifiers, but one nonlinear optical process which is of particular interest is Second Harmonic Generation (SHG).

1.3.1 Second Harmonic Generation

Second Harmonic Generation is a nonlinear optical process by which photons encounter a crystal with the appropriate $\chi^{(2)}$ tensor and produce photons at twice the frequency (or half the wavelength). Among other applications, it is commonly employed in commercial green laser pointers, to convert 1064 nm light from a common solid-state neodymium laser into 532 nm light[15].

SHG a second-order process, governed by the $\chi^{(2)}\mathbf{E}^2$ term in the nonlinear polarization from Equation 1.8. For a simple case, when a pump wave $\mathbf{E} = E\cos(\omega t)$ first encounters the crystal, the second-harmonic generation is easily seen:

$$\begin{aligned}\mathbf{P}_{NL} &= \epsilon_0\chi^{(2)}\mathbf{E}^2 = \epsilon_0\chi^{(2)}E^2\cos^2(\omega t) \\ &= \frac{1}{2}\epsilon_0\chi^{(2)}E^2(1+\cos(2\omega t))\end{aligned}$$

In practice, conversion does not occur with 100% efficiency. The field equations and propagation become more complicated as SHG progresses through the crystal, some input light is left unconverted, and higher harmonics are also generated, especially as input power increases and the higher-order terms become even more significant. An illustration of the inputs and outputs of a crystal of Periodically Poled Lithium Niobate (PPLN) doubling 1550 nm light is shown in Figure 1-2.

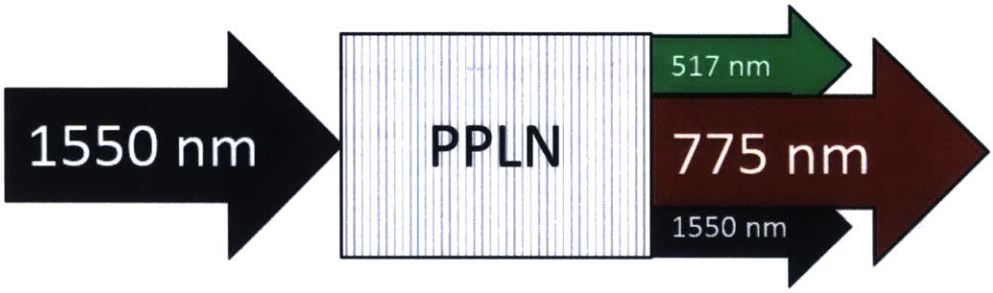

Figure 1-2: 1550 nm light being passed through a properly-tuned crystal of PPLN. Note that most light is doubled to 775 nm, but that some 1550 nm light passes straight through, and some parasitic third-harmonic generation is also occurring.

1.3.2 Quasi-Phase Matching

One critical element of second-harmonic generation (and any nonlinear process in which multiple frequencies are present) is phase-matching. The index of refraction of a material is dependent on wavelength, and so as light passes through a material and undergoes SHG, the input light and the second harmonic move at different speeds and so become out of phase with each other in a matter of micrometers (called the coherence length). In some materials, such as Periodically Poled Lithium Niobate (PPLN), this phase mismatch is neutralized by quasi-phase matching. The crystal is exposed to electromagnetic fields during manufacturing that cause the nonlinear optical coefficients to form domains of opposite signs. This causes the second harmonic to alternate between being faster and slower than the input wave, causing them to remain in-phase on average and maximizing conversion efficiency. This process is illustrated in Figure 1-3.

The poling period must be carefully controlled, and depends on the wavelength being doubled. If the phase mismatch is not incremented and decremented by the same amount over alternate poling domains, then the phase mismatch will eventually grow enough to result in destructive interference. In practice, crystals can be manufactured with multiple tracks of different poling periods for different wavelength ranges, and thermal control can be employed to expand and shrink the crystal and its poling for further adjustment.

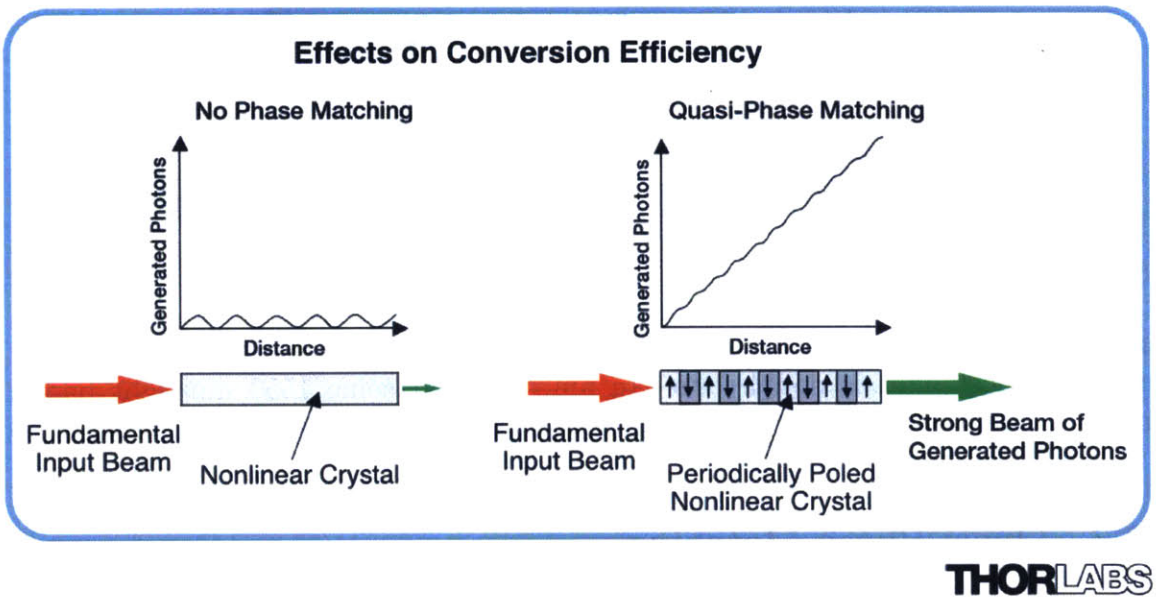

Figure 1-3: An illustration of the effect of periodic poling and quasi-phase matching on SHG conversion efficiency. [1]

1.4 Avalanche Photodiodes

Avalanche Photodiodes (APDs) are used in the planned NODE optical receiver. APDs are photodiodes with a reverse bias voltage applied, so that when photons encounter the semiconductor and excite individual electrons, an easily-detected "avalanche" current is produced.[3] The semiconductors and architectures used for APDs are selected based on the wavelengths and bandwidths of interest; for example, Indium Gallium Arsenide (InGaAs) is used for infrared wavelengths (800-2500 nm)[16], and silicon is used for visible and near-infrared wavelengths (200-1200 nm).[17]

One of the noise sources of APDs is "excess noise", which scales with the APD gain M_{APD} and a factor k_A which depends on the semiconductor ($k_A = 0.02$ for silicon, and $k_A = 0.45$ for InGaAs)[18]. The relationship between excess noise F_A and gain is illustrated in Equation 1.9.[19]

$$F_A = k_A M_{APD} + (1 - k_A)(2 - 1/M_{APD}) \tag{1.9}$$

This excess noise grows faster than gain does, so for some received power on the

detector, there is an ideal gain which maximizes Signal-to-noise ratio (SNR). Because silicon APDs have a lower k_A than InGaAs, their excess noise is lower and they can be operated at higher gains. Typical APD gains are around 10 for InGaAs and 100-150 for silicon (and upwards of 500 in some applications).[18]

1.4.1 Geiger-mode APDs

When APDs are operated at voltage biases above the breakdown voltage, a single photon is capable of exciting an avalanche current. In this regime, the concept of "gain" is not very meaningful, as each incident photon is detected. These so-called "Geiger-mode APDs" are sometimes referred to as photon counters, and they are applied for communication links where there are very few photons arriving, such as LLCD.[7] In ground testing, GM-APDs have closed links with as few as 1.5 photons per bit.[20]

The signal to noise ratio of GM-APDs depends on the statistics of photons received and counted vs. the dark count, or spurious electron excitations that were not precipitated by photons. Kolb[21] (RIT) provides a formula for the SNR of a Geiger-mode APD:

$$SNR = \frac{PDE \cdot \lambda_p \cdot n_{gates}}{\sqrt{P_1 P_0 \left(1 + 2\frac{p_{aft} e^{-\lambda}}{1 - p_{aft} e^{-\lambda}}\right) \left[\frac{1 - p_{aft}}{P_0(1 - p_{aft} P_1)}\right]^2 n_{gates}}} \tag{1.10}$$

Where:

λ_p is received photons per gate

λ_d is the dark count rate (charge carriers per gate, given by the datasheet)

PDE is the photon detection efficiency

$\lambda = PDE\lambda_p + \lambda_d$ is the average number of charge carriers per gate[3]

n_{gates} is the number of gates

[3]Not to be confused with wavelength, which is what λ represents in the rest of this research.

p_{aft} is the probability of "aftercounts", spurious counts that one gate can trigger in the next

$$P_1 = \frac{1-e^{-\lambda}}{1-p_{aft}e^{-\lambda}} \text{ [n.d.]}$$

$$P_0 = 1 - P_1 = \frac{e^{-\lambda(1-p_{aft})}}{1-p_{aft}e^{-\lambda}} \text{ [n.d.]}$$

A "gate" in this case refers to a sample from one cell of a given duration. Commercial photon-counting modules incorporate several hundred or thousand photodiodes[22, 23], so that they can achieve good gate counts to improve SNR while keeping short gate durations. Given some received power P_r, slot rate T_s, pixel count n_{pix}, and photon energy $\mathcal{E}$, $\lambda_p = P_r T_s/(\mathcal{E} n_{pix})$. PDE, p_{aft}, and λ_d are taken from product datasheets[22, 23].

The SNR of a GM-APD will clearly be negatively impacted as the amount of incoming photons (λ_p) decreases, but this formula also shows how a detector can saturate. As the amount of received photons increases, λ increases and $e^{-\lambda}$ approaches zero. P_1 converges to 1 and P_0 converges to zero, and SNR becomes proportional to $\sqrt{\frac{P_0}{P_1}}$. At this point, so many photons are incident that the detector cannot distinguish pulses.

1.5 Literature Review

The literature review is divided among the same fields laid out above: laser communication, nanosatellites, and nonlinear optics.

1.5.1 Review of space-based laser communication

Near-Earth Laser Communication, ed. Hemmati[24], and *Optical Communication Receiver Design*[25] (Alexander) are seminal works on optical communication. Alexander's analysis of receiver statistics and Hemmati's atmospheric property figures are used in this research.

Moision and Xie[26] and Moision and Farr[6] (JPL) derive link budget equations specific to laser communication using pulse-position modulation (as opposed to radio

communication). Some notable differences between laser and radio communication is that direct-detection laser communication with PPM is bounded by three factors, depending on the SNR. In particular, the channel capacity may be limited by background noise, available signal power, and eventually by the slot rate and PPM order as signal power increases.

For links where there are hundreds of photons per bit, and channel capacity is limited by the signal modulation, a more useful metric can be the margin between received power and the power required to distinguish pulses from the background. Emily Clements[27] builds on work by Kingsbury[8] to analyze the effects of uncertainties in link design parameters on the link margin.

Govind Agrawal's (University of Rochester) lectures on optical communication[19] covers the receiver in more detail. In particular, the dominant noise source of avalanche photodiodes depends on the gain with which the APD is used. For a given APD, there is an optimum gain which balances the need to amplify the incoming signal against the growth of thermal noise with gain. Silicon photodiodes (sensitive from 250-1000 nanometers[28]) have a higher optimum gain than InGaAs (sensitive from 900-1700 nanometers[28]) because of their lower noise factor.

Several vendor information sheets from Hamamatsu (Hamamatsu City, Japan) and Excelitas (Waltham, MA) were consulted for general background on APDs[3, 18] and for details on specific silicon[17, 22] and InGaAs[16] APD models for use in the link budget analysis.

One outstanding achievement of laser communication is the Lunar Laser Communication Demonstration (LLCD), as reported by Boroson et al.[7] LLCD was a payload carried on NASA's Lunar Atmosphere and Dust Environment Explorer (LADEE) mission, and it successfully achieved an error-free communication rate of 622 Mbps from lunar orbit, transmitting 0.5 W (optical) at 1550 nm to an array of four 40-cm receive telescopes. Intersatellite crosslinks have also been demonstrated between large satellites in e.g. the Near Field InfraRed Experiment (NFIRE), which achieved data rates of 5.625 Gbps across 5100 km.[29, 30] NFIRE transmitted 0.7 W (optical) at 1064 nm to a 125 mm receive telescope on the German TerraSAR-X satellite.[30]

1.5.2 Review of optical communication on nanosatellites

Several nanosatellites which demonstrate optical communication technologies have been or are being built and launched. The Optical Communication and Sensor Demonstration (OCSD) mission by NASA and The Aerospace Corporation[31] uses a custom 14 W (optical power) laser at 1064 nm to a 30 cm telescope, to achieve planned data rates in excess of 5 Mbps. OCSD-A suffered a problem with its attitude control system[4] that prevented it from testing its optical communication payload, but OCSD-B and -C are scheduled for launch in summer 2016 to perform an intersatellite link test.

MIT's Nanosatellite Optical Downlink Experiment[8] is planned to use a COTS 200 mW (optical power) laser at 1550 nm to achieve data rates in excess of 10 Mbps to a 30 cm telescope. The major difference in architecture that will allow NODE to achieve similar data rates for orders of magnitude less power is that NODE includes a Fine steering mirror (FSM) to allow finer pointing than can be achieved by a CubeSat's actuators alone. This allows the beam to be narrower to achieve sufficient SNR to achieve multi-Mbps data rates.

NODE's communication technology is forming the basis of two other projects: KitCube[33, 12], a 6U CubeSat intended to achieve 1 Mbps of downlink speed from the Moon, and FLARE[2], a pair of 6U CubeSats which will demonstrate an intersatellite crosslink.

In both OCSD and NODE, the laser system must fit into less than 1U of the satellite, and with follow-up missions involving intersatellite cross-links, there are benefits to be obtained from small frequency-agile systems.

1.5.3 Review of nonlinear optics technologies relevant to FSO

Bahaa Saleh and Marvin Teich's *Fundamentals of Photonics*[13, 14] covers the fundamentals of nonlinear optics, including the nonlinear constitutive relation which links

[4] An ACS software update was executed over multiple ground-station passes. Partway through the planned series of passes, the ACS motherboard rebooted, and was not able to initialize in its partially-updated state.[32]

nonlinear behavior in material polarization to the displacement field. Some of the implications that this has on the practical construction and use of nonlinear crystals is discussed in material from Thorlabs (Newton, New Jersey) and Covesion (Hampshire, United Kingdom), manufacturers of nonlinear crystals[1, 34].

Bill Farr inspired and was a mentor for some research conducted in this thesis, studying the conversion efficiency of PPLN to assess its utility in improving data rates for Mars-Earth laser communication links. In this work, we assess whether its benefits are also applicable for Earth orbits, and that the ability to switch frequencies with the same trasmit hardware may be particularly beneficial for constrained CubeSat platforms.

Cheng *et al.*[35] (Centre for Quantum Technologies, National University of Singapore) describe a proposed and constructed mission to use a 1U CubeSat to carry a nonlinear optical element into space. This optical element was not intended for frequency-doubling, but rather "halving" – producing entangled pairs of half-frequency daughter photons from single input photons, to demonstrate technologies that could be used to produce entangled photons for space-based quantum key distribution systems. Unfortunately, the launch failed and the satellite was lost (a successor, "SpooQy-Sat", is planned to launch in 2017[36]), but the setup of a thermally-controlled nonlinear optical element is similar to that proposed for the Frequency-Doubling Optical Transmitter (FDOT). Bedington *et al.*[36] (Centre for Quantum Technologies, National University of Singapore) note that intersatellite crosslinks of entangled photons could be the backbone for "long-baseline test[s] of quantum correlations", as well as enabling quantum key distribution in a manner which is much less vulnerable to side-channel attacks than terrestrial quantum photon sources.

There are potential science applications for frequency-agile communications lasers. For example, optical parametric oscillation (to produce longer wavelengths) may generate wavelengths useful for probing atmospheric composition.[37] Having a satellite guidestar that can generate multiple wavelengths simultaneously (as nonlinear optical elements can, if they are operated at slightly off-nominal conditions – see Figure 1-2) is also valuable for photometric calibration of telescopes.[38]

1.6 Nonlinear Optics for Frequency-Doubling in Nanosatellite Laser Communication

The focus of this research is on the intersection of free-space laser communication, nonlinear optics, and nanosatellites: a Frequency-Doubling Optical Transmitter (FDOT) for nanosatellites. The concept of operations is that a nanosatellite can use a frequency-doubling nonlinear optical element to have the capability to transmit on two different wavelengths using a common seed laser, modulator, and amplifier (as opposed to having to carry an entire second laser system). A block diagram illustrating the system in two modes of operation is shown in Figure 1-4, and an estimated mass budget is presented in Table 1.1. Estimated values are derived from the densities of gallium arsenide and lithium niobate (the active components of the polarization modulator and frequency-doubling crystal, respectively) and part dimensions. Structural and fiber masses are not included, as their mass is expected to be similar to those of the host laser system.

Table 1.1: Estimated mass budget of FDOT.

Component	Mass (g)	Notes
Polarization modulator[39]	45	Estimated
Collimator (2x)	4×2	Measured
Crystal and TEC	< 1	Estimated
Total	65	54 g with 20% margin

The advantage that this approach has is that it allows a system to use the best features of each frequency for the situations in which they are favored. For example, a system operating at 1550 nm is compatible with commercial optical communication hardware, which can simplify ground-station design, while better detectors are available at 775 nm. Ground stations can sustain large apertures and other technologies such as cryo-cooling to improve SNR, but such measures are not feasible for space systems on volume-constrained nano- and microsatellites.

The use of frequency-doubling allows a satellite to have access to both wavelengths

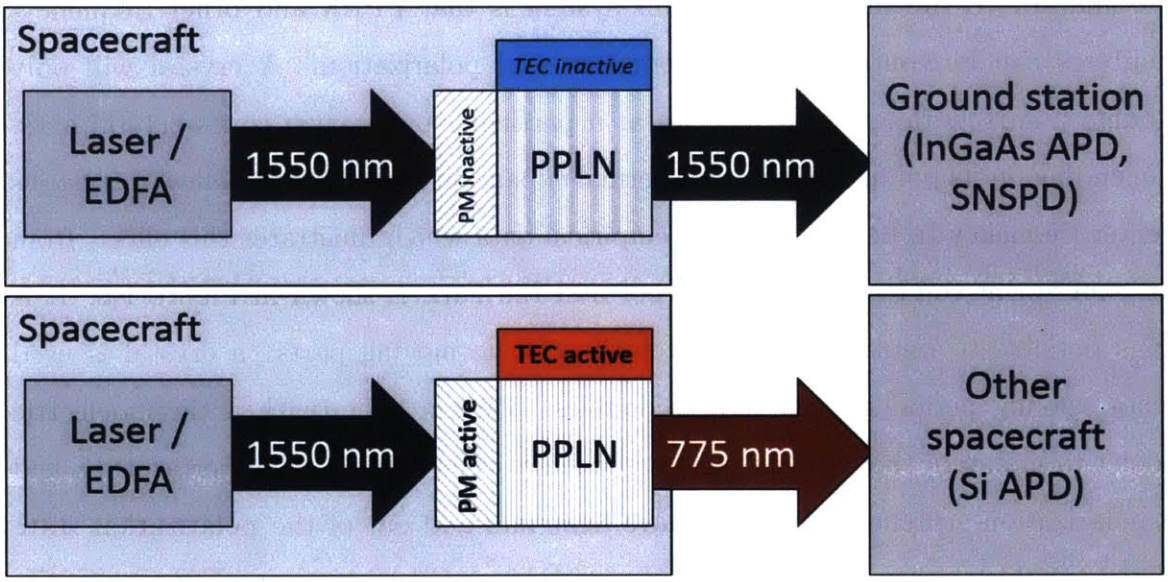

Figure 1-4: An illustration of a frequency-doubling optical transmitter in two modes of operation. At the top, the nonlinear element is inactive, and the 1550 nm laser passes through unmodified. In the second mode, the element is active and doubles the light passing through it to 775 nm.
TEC: Thermoelectric cooler
PM: Polarization modulator

for less than the cost (in terms of size, weight, and power) of having one conventional system for each. One such trade, considering 1550 nm and 775 nm with a PPLN doubler, is laid out in Table 1.2. There are many other trades to be made, both in terms of materials and frequencies to be used, such as Potassium Titanyl Phosphate (KTP) and 1064/532 nm, and in terms of system architecture, such as the choice of linear-mode APDs, Geiger-mode APDs, or superconducting nanowire single photon detectors.

The key to the functioning of this system is that PPLN and other frequency-doublers can be controlled by temperature and polarization. A crystal will only double a narrow range of frequencies at a particular orientation to its crystal axes, depending on its poling period, and thermal expansion is exploited to allow a crystal's center frequency to be tuned. Some empirical data which illustrates this effect, from an experiment conducted by the author and Bill Farr, is shown in Figure 1-5. It is thus possible to implement the switching with no moving parts: a crystal is used whose poling period is such that it doubles 1550 nm light (with a thermoelectric cooler to maintain the crystal's center frequency when SHG is being performed), and a polarization switcher is used to move light into and out of the polarization state that is doubled.

For polarization-modulation systems, two crystals at right angles to each other would be required, and the operating point of the crystals would have to be moved well away from the ambient temperature of the spacecraft. Crystal ovens intended for laboratory use require several watts to operate[34], which can be improved in the space environment, but to simplify the analysis of the power cost of the frequency-doubling system, the laser is assumed to use pulse-position modulation, so that polarization could be used to control the SHG conversion itself.

The goal of this research is to develop tools to explore the laser communication trade space expanded by this option and determine where improvements of at least 3 dB in link margin and/or data rate over state-of-the-art 1550 nm links can be obtained.

Table 1.2: A brief qualitative trade to motivate the utility of frequency-doubling optical transmitters.

	Pure 1550 nm	**Pure 775 nm**	**Hybrid w/ Freq. Dbl.**
Positive	COTS telecom hardware available and inexpensive Lower photon energy means more photons generated, reduced shot noise	Silicon APDs have less thermal noise than InGaAs [18, 19] Narrower diffraction limit	Takes advantage of the advantages of both wavelengths
Negative		Falls within FAA definition of "visible" [5] – extra reg. overhead to downlink Most current, recent, and planned ground stations operate at NIR, e.g. OCTL[40], LLGT[7], and BridgeSat (based on AeroCube[41]) Greater sky radiance at visible wavelengths (ground stations only)[24, Fig. 8.16]	Conversion is not 100% efficient
Mass	200 g (MOPA)[8, Tab. 3.5], for laser parts only	100 g (HPLD, max bandwidth $<$ 100 MHz)[8]	200 + 65 g (see Table 1.1)

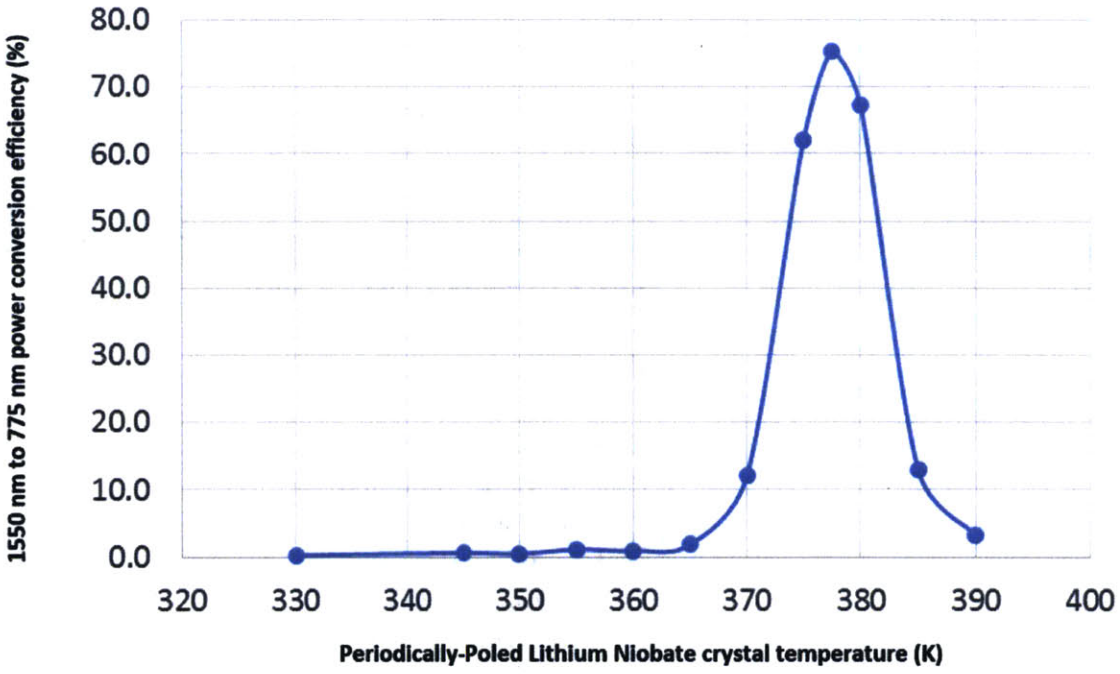

Figure 1-5: SHG conversion efficiency vs. temperature for a PPLN crystal. From research mentored by Bill Farr.

Chapter 2

Approach

2.1 Current tools

Link budgets for direct-detected laser communication with pulse position modulation (PPM) do not behave in the same way as link budgets for radio communication. Moision and Xie have developed an approximate channel capacity equation that incorporates the three major constraints on a lasercom channel: signal power, noise power, and finally, the modulation bandwidth itself.[26] These constraints are represented in order by the terms in the denominator of the channel capacity equation, Equation 2.1.

$$C_{opt} \approx \frac{1}{\mathcal{E} \ln 2} \left(\frac{P_r^2}{P_r \frac{1}{\ln M_{PPM}} + P_n \frac{2}{M_{PPM}-1} + P_r^2 \frac{M_{PPM} \cdot T_s}{\mathcal{E} \ln M_{PPM}}} \right) \tag{2.1}$$

In this equation, C_{opt} is the optical link capacity (bits-per-second), P_r and P_n are received signal and noise powers respectively (W), M_{PPM} is the PPM order, T_s is the slot width, and $\mathcal{E} = h\nu = hc/\lambda$ is the photon energy.

For NODE and other links where the received signal power is on the order of hundreds of photons-per-bit, the predominant constraint is the third, where the channel capacity is capped by the bandwidth of the laser modulation (the slot rate and PPM order). In such circumstances, it is most helpful to calculate the margin of received power above the minimum power required to statistically distinguish pulses at that

slot rate and PPM order above the noise from the detector and the sky, with some desired bit error rate.

The design space exploration tool used for this research is based on link-budget analysis performed by Ryan Kingsbury for his thesis[8] and extended by Emily Clements to analyze the sensitivity of the link margin to variations of several input parameters[27].

The received power is calculated from the Friis transmission equation, represented (in dB form) in Equation 2.2:

$$P_r = P_t + G_t + G_r - L_t - L_r - L_{fs} - L_{atm} - L_{pt} \tag{2.2}$$

Where P_r is recived power at the detector, P_t is power transmitted, G_t and G_r are transmit and receive gain, L_t and L_r are transmit and receive losses (from e.g. splices and beam splitters), L_{fs} is free-space loss, L_{atm} is atmospheric loss, and L_{pt} is pointing loss.

Receive gain has a dependency on wavelength:

$$G_r = 20 \log_{10} \left(\frac{\pi D_r}{\lambda} \right) \tag{2.3}$$

Where D_r is the receive diameter and λ is the received wavelength.

G_t has a similar form when the transmitter is diffraction-limited, but NODE and FLARE's beamwidths (HPBW) are set by collimation optics[8, 2], and so it has the following form:

$$G_t = 10 \log_{10} \left(\frac{2}{1 - \cos(HPBW/2)} \right) \tag{2.4}$$

Free-space loss also has a dependency on wavelength, which cancels out the receive gain's dependency:

$$L_{fs} = 20 \log_{10} \left(\frac{\lambda}{4\pi R} \right) \tag{2.5}$$

Atmospheric loss depends on wavelength, but is not a factor for an intersatellite crosslink. The transmit and receive losses are assumed to be identical for both wave-

lengths – on the transmit side, the same optical hardware is used for both wavelengths, and the different receivers used are assumed to use the same architecture.

Pointing loss comes from the reduction of laser power delivered to the detector resulting from failure to center the beam – for instance, if the pointing is off by the half-power beamwidth, then there will be a 3 dB loss. For diffraction-limited transmitters, the narrower beam from the shorter wavelength would exacerbate pointing losses, but because NODE's beamwidth is defined by a collimator, the beams will be of the same width and the pointing losses will also be the same. Alternatively, a diffraction-limited system could use the wider beam at 1550 nm for beacon acquisition, and then switch to the narrower 775 nm beam for communication.

Because NODE and FLARE use PPM encoding, the average received power is not representative of the actual signals which must be distinguished. For a given PPM order M_{PPM}, the average received power is as follows:

$$P_{av} = P_r = \frac{1}{M_{PPM}} P_{peak} + \frac{M_{PPM} - 1}{M_{PPM}} P_{peak} \times \frac{1}{ER} \tag{2.6}$$

From this, we can compute two power ratios of the peak and off-pulse received powers to average power:

$$PR_{peak-av} = \frac{P_{peak}}{P_{av}} = \left(\frac{1}{M_{PPM}} + \frac{M_{PPM} - 1}{M_{PPM} \times ER} \right)^{-1} \tag{2.7}$$

$$PR_{off-av} = \frac{P_{off}}{P_{av}} = \frac{1}{ER} PR_{peak-av} = \left(\frac{ER}{M_{PPM}} + \frac{M_{PPM} - 1}{M_{PPM}} \right)^{-1} \tag{2.8}$$

The power received during a pulse is thus $P_{peak} = P_{av} PR_{peak-av}$, which produces a photocurrent of $\mu_{i,on} = M_{APD} R_{APD} (P_{peak} + P_{back})$ given APD gain M_{APD} and responsivity R_{APD} and background power P_{back}[1]. Likewise, a photocurrent of the off-slots $\mu_{i,off} = M_{APD} R_{APD} (P_{off} + P_{back})$ can also be calculated.

These form the centers of two Gaussian distributions[2], which have standard devi-

[1]Neglected for this analysis, as the background of a space-to-space link is assumed to have negligible atmospheric noise – otherwise, background noise is worse at 775 nm than 1550, 70 vs. 4 W/(m^2-sr-μm)[24, Fig 8.16]

[2]As photons and electrons are discrete entities, the probabilities obey Poisson statistics, but when

ations σ^2_{on} and σ^2_{off}:

$$\sigma^2_{on} = 2q \times M_{APD} \times NEB \times F_A \times \mu_{i,on} + \sigma^2_{amp} \tag{2.9}$$

$$\sigma^2_{off} = 2q \times M_{APD} \times NEB \times F_A \times \mu_{i,off} + \sigma^2_{amp} \tag{2.10}$$

Where q is the charge of the electron, NEB is the noise equivalent bandwidth (1.5x the slot clock rate, per Kingsbury[8]), and F_A is the excess noise factor, calculated from Equation 1.9. σ^2_{amp} is amplifier noise, which is scaled by the noise equivalent power NEP:

$$\sigma^2_{amp} = (NEP \times R_{APD} \times M_{APD})^2 \tag{2.11}$$

Noise equivalent power is itself defined by the equivalent amount of photon power required to produce an SNR equal to 1. This is driven by thermal noise in the detector[42]:

$$NEP = \sqrt{\frac{4k_B T F_n}{R_{in} R^2_{APD}}} \tag{2.12}$$

Where k_B is the Boltzmann constant, T is the APD temperature, F_n is the noise figure of the second-stage (electrical) amplifier (measured empirically by Ryan Kingsbury to be 4.3 for the case of NODE[8]), R_{in} is the input resistance of the second-stage amplifier (usually 50 Ω), and R_{APD} is the responsivity of the APD (A/W).

The bit error rate is defined by the overlap of the two distributions, as shown in Figure 2-1.

The probability of a bit error is a function of the Q-factor[8]:

$$Q = \frac{\mu_{i,on} - \mu_{i,off}}{\sqrt{\sigma^2_{on} + \sigma^2_{off}}} \tag{2.13}$$

there are enough photons-per-bit, the two are approximately equal, and the Gaussian statistics are simpler. Additionally, using the Gaussian distribution will lead to an overestimate of the power required to achieve a given bit error rate, so it is valid to use that approximation for calculating margins.[25]

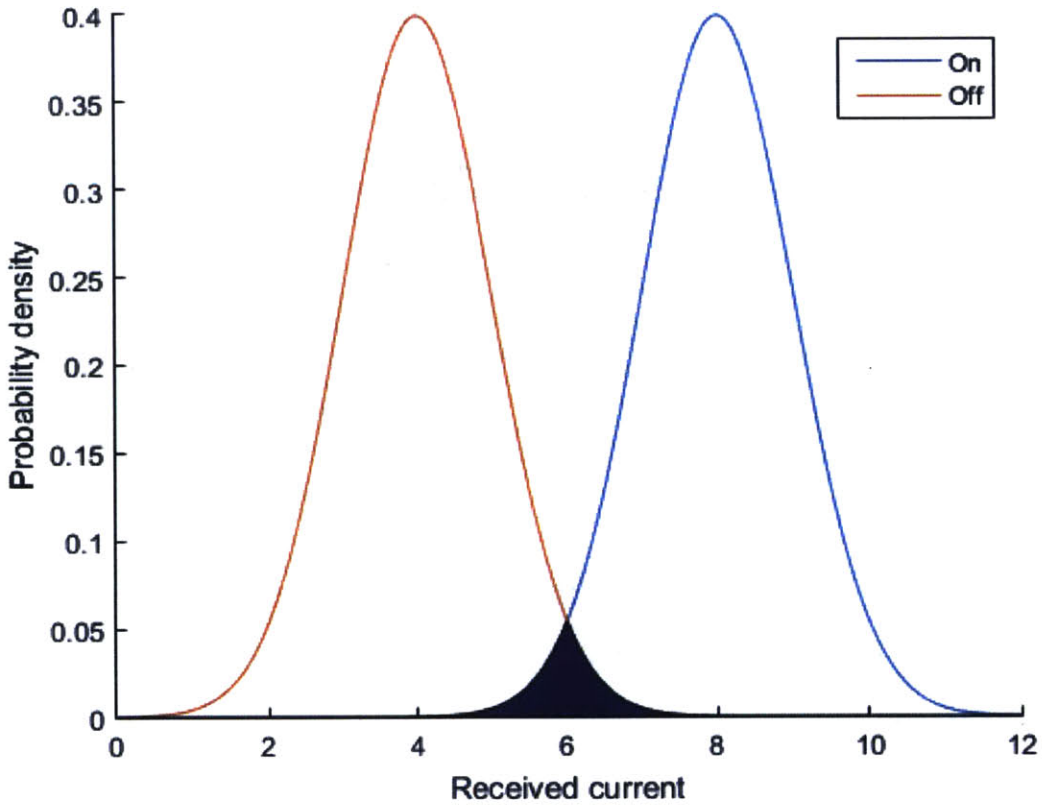

Figure 2-1: Notional distributions of APD currents for on- and off-signals. The overlap area is where bit errors can occur.

$$BER = \frac{M_{PPM}}{4} \operatorname{erfc} \frac{Q}{\sqrt{2}} \tag{2.14}$$

Therefore, if a desired BER is known (e.g. 10^{-4}, which can be compensated with coding), and PPM order M_{PPM} is given, the photocurrent (and thus photon power) required to distinguish on-slots from off-slots at the desired bit error rate can be calculated:

$$Q_{req} = \sqrt{2} \operatorname{erfc}^{-1} \frac{4 \times BER}{M} \tag{2.15}$$

$$\mu_{i,on,req} = Q_{req} \sqrt{\sigma_{on}^2 + \sigma_{off}^2} + \mu_{i,off} \tag{2.16}$$

$$P_{req} = \frac{1}{PR_{peak-av}} \left(\frac{\mu_{i,on,req}}{M_{APD} R_{APD}} - P_{bckg} \right) \tag{2.17}$$

Given the required power from Equation 2.17 and the received power from Equation 2.2, the margin is thus calculated:

$$\text{Margin} = 10 \log_{10} \left(\frac{P_r}{P_{req}} \right) \tag{2.18}$$

2.2 System overview

The FLARE is a mission under development at MIT consisting of two 6U CubeSats which will, among other tasks, demonstrate a laser crosslink at a range of at least 200 km. The current design includes an 85-mm receive aperture and a 1550 nm laser transmitter based on COTS telecom hardware.[2] The satellite, with its receive aperture front and center, is depicted in Figure 2-2.

The design parameters of its link budget are laid out in Table 2.1. Because FLARE is still in formulation, many factors have been sourced from NODE for the base case. Some of these parameters will be varied for certain cases, such as beamwidth and laser wavelength. Because the SHG step occurs after laser modulation and amplification,

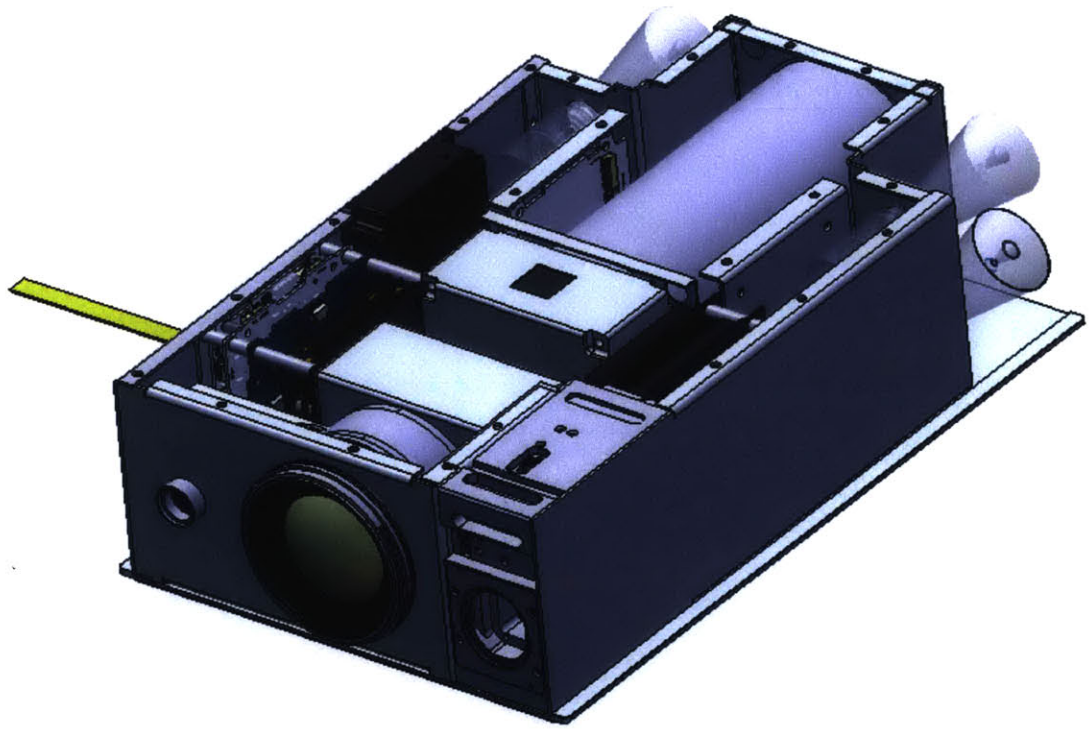

Figure 2-2: Cutaway Diagram of FLARE.[2] Dimensions: $10 \times 20 \times 30$ cm. The receive aperture depicted is an 85 mm $f/1.8$ camera lens. This is not the final design of FLARE, but will be used as the notional design for all analyses.

the extinction ratio of 42 dB is inherited for the 775 nm cases.

Table 2.1: Link budget inputs from FLARE used for the purpose of this analysis.

PPM Order	64[8]
Slot Rate	200 MHz[8]
Average optical output power	200 mW[8]
Laser wavelength	1550[27] / 775 (using FDOT) nm
Extinction ratio	42 dB[27]
Half-power beamwidth	2.26 mrad[27]
Path length	200 km[2]
Receiver aperture	85 mm[2]
Receiver focal length	153 mm ($f/1.8$ lens)[2]

Chapter 3

FDOT Analysis

3.1 Developed tools

In this section we describe our analysis of the performance of FDOT on the link margin of a nanosatellite crosslink. The frequency-doubling analysis tool performs two parallel analyses for the two cases: a baseline case at 1550 nm, and a second case at 775 nm, which takes into account the loss of electrical power to the laser due to the oven or polarization switcher, the loss of laser power due to conversion inefficiency, the different noise and gain characteristics of silicon vs. InGaAs APDs, and the different sky background noise at 1550 and 775 nm (where applicable).

APD noise is dominated by thermal noise at low gains (of roughly constant power) and shot noise at high gains (which grows faster than gain, due to the excess noise factor). The optimum gain is high enough to amplify the signal above thermal noise, but not so high that the excess noise grows out of control. A notional diagram of the optimum gain is shown in Figure 3-1.

Note that the optimum gain depends on the incoming signal power. The optimum gain is given by Equation 3.1[3]:

$$M_{APD,opt} = \left(\frac{4k_B T}{q(I_l + I_{dg}) x R_L} \right)^{1/(2+x)} \tag{3.1}$$

Where k_B is the Boltzmann constant (1.38×10^{-23} J/K), T is the APD temperature

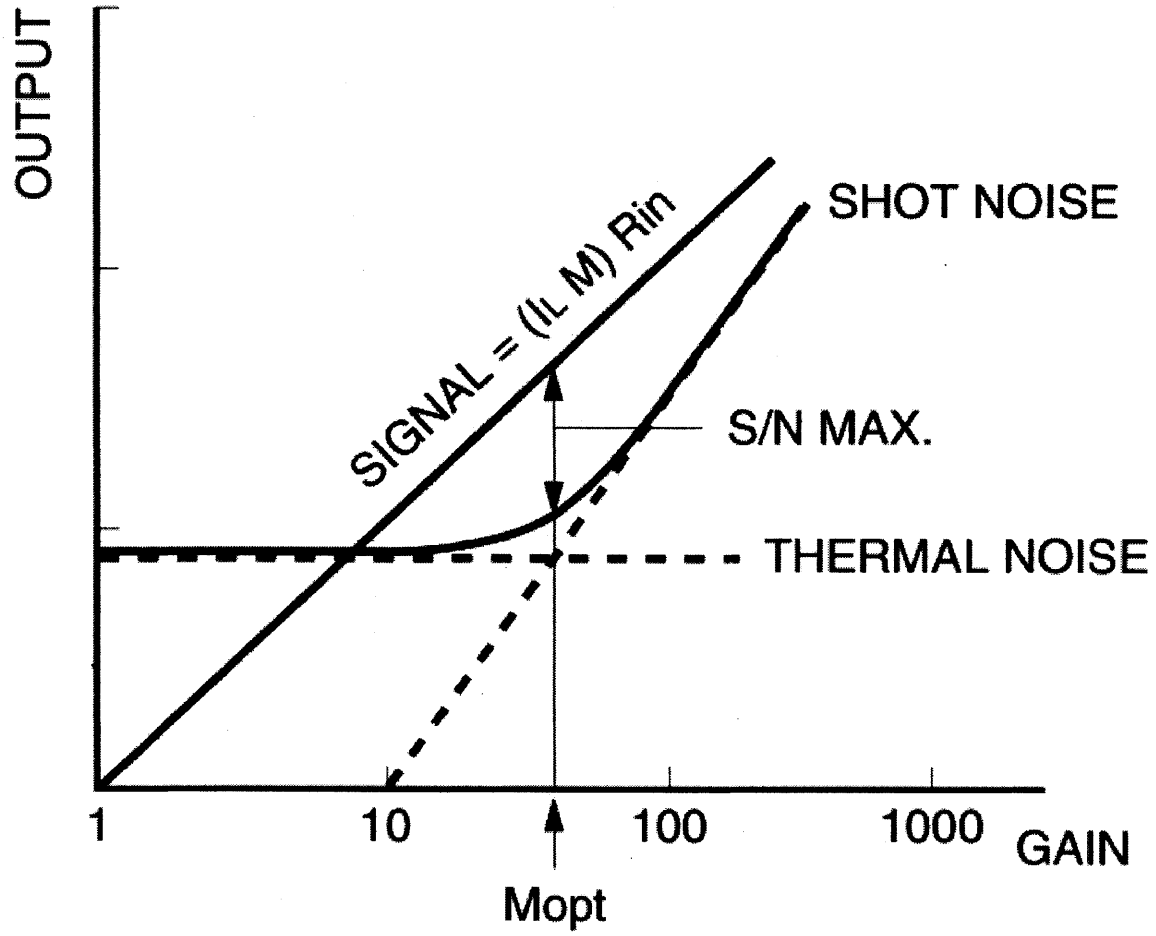

Figure 3-1: A notional diagram of SNR vs. gain for an APD, from Hamamatsu[3]. Note that R_{in} is the input resistance of the next-stage amplifier, converting a current signal into a voltage signal.

(K), q is the elementary charge (1.602×10^{-19} C), and x is an empirically-determined excess noise coefficient for an APD architecture (0.3 for silicon, 0.45 for InGaAs[18]). It is distinct from k_A; where k_A is used in the exact formulation of excess noise in Equation 1.9, x is used in an approximation $F_A \approx M_{APD}^x$ which is more amenable to differentiation, which is used to derive the optimum APD gain.[3]

I_l and I_{dg} are the photocurrent produced by incident photons (at unity gain, or $R_{APD}P_{rec}$) and dark current subjected to gain, respectively. (There is also I_{ds}, dark current which is not subject to gain, but because the APDs are operated at gains much greater than 1, it is negligible.)

The dark current and responsivity are parameters of the specific APD. For this analysis, two APDs were selected as bring generally applicable for optical communication and having readily accessible datasheets: the InGaAs G8931-04[16] and the silicon S12023-10[17]. The optimum gain curves are plotted in Figure 3-2 (with the G8931-04 plotted alone in Figure 3-3, for visibility).

The other new factor included in the analysis is the power required to use second-harmonic generation. A laser system can be characterized by its electrical power budget P_{elec} and wall-plug efficiency η_{wp}, and will produce $\eta_{wp}P_{elec}$ watts of optical power. For NODE's Master Oscillator Power Amplifier (MOPA) architecture, this efficiency is 200 mW / 5.7 W = 3.5%.[8]. The power required to use second-harmonic generation, P_{shg}, will reduce the available power for the laser, resulting in an output optical power of $(P_{elec} - P_{shg})\eta_{wp}$.

For this analysis, polarization control was assumed, because the power consumption of a 3.3V polarizer with 50Ω resistance is easily calculated (0.22 W, with a further 0.4 W for the TEC to compensate for the ambient spacecraft temperature to control the center frequency of the PPLN crystal[8]). SHG is sensitive to polarization as well as poling period and wavelength, so this provides a low-power means of control. It does induce a 3 dB transmitter optical loss (L_T), and would not be possible on a system using polarization shift keying (PolSK) modulation, as there would be a crystal dedicated to each polarization component.

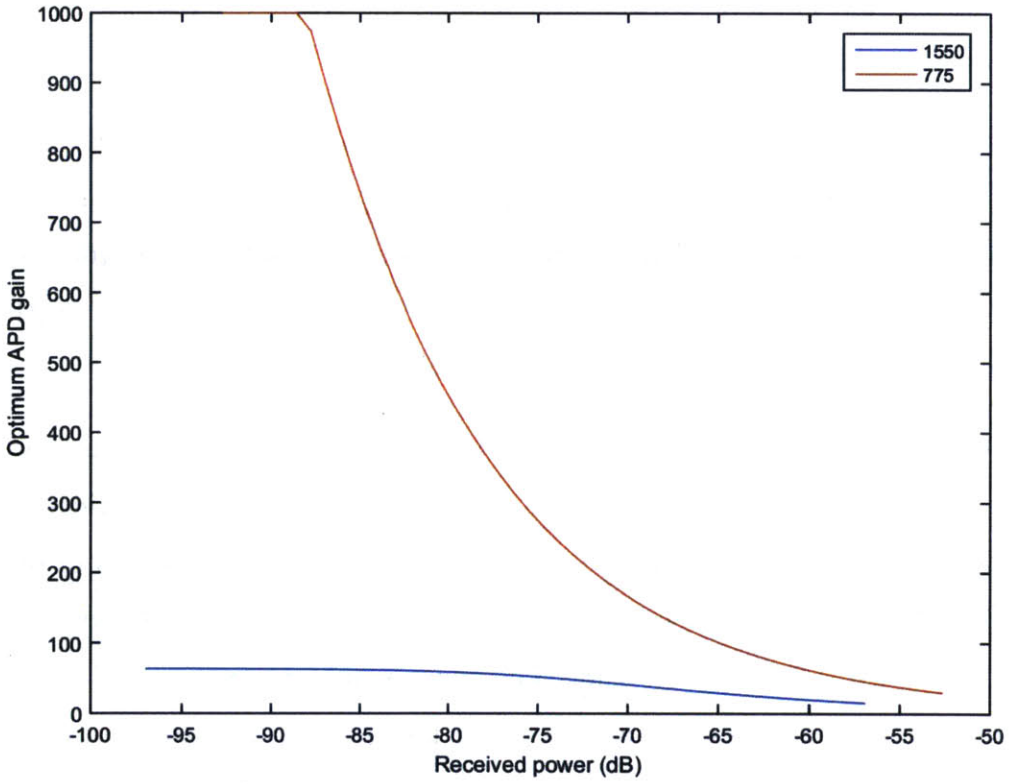

Figure 3-2: Optimum gain vs. received power for silicon APD S12023-10 and InGaAs APD G8931-04.

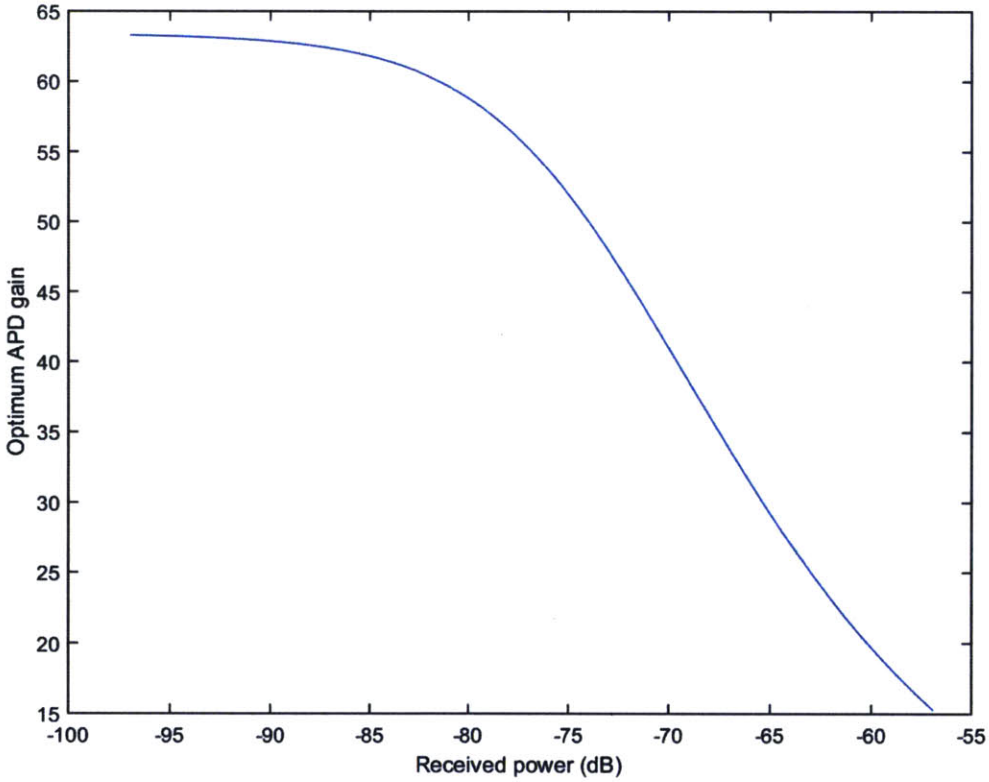

Figure 3-3: Optimum gain vs. received power for InGaAs APD G8931-04.

3.1.1 Geiger Mode APD simulation

Another simulation tool was created to explore the design space of Geiger mode APDs. In this regime, with fewer than 100 photons per bit, the assumption that channel capacity is limited by modulation bandwidth is no longer valid, as background noise is no longer negligible. Using the same calculation of P_r as in Equation 2.2, and the SNR calculation from Equation 1.10, noise power $P_n = \frac{P_r}{SNR}$, which is used in the channel capacity equation (Equation 2.1) to calculate the final bitrate.

3.2 Cases studied

3.2.1 FLARE

FLARE was the primary case studied, as it is a project early enough in development for this analysis to be relevant, and it offers the most favorable circumstances for SHG to be applied: atmospheric background noise can be neglected for a space-to-space link ASDF, and the limited detector volume restricts the more advanced detector technologies that silicon APDs would otherwise have to compete with.

The electrical power budget of the laser communication system was varied from 5 to 50 W to encompass the range typified by NODE (5.7 W)[8] and OCSD (56 W)[31]. The link range was varied from 100 km to 10,000 km to capture the closest and most distant encounters that could reasonably be expected in LEO (the maximum distance between two satellites seeing each other over the horizon of the Earth in 1,000 km orbits is approximately 7,400 km).

3.2.2 Diffraction-limited FLARE

FLARE's transmit beamwidth is determined by a collimator, while the beamwidth of a diffraction-limited system is proportional to D/λ, which improves by a factor of 2 with SHG (thus improving gain by a factor of 4, or 6 dB). During a conversation with Bill Farr, it was suggested that a second case should be run to capture this improvement. For this case study, the system was assumed to have an aperture

diameter of 1.67 mm, which produces a 2.26 mrad wide Airy beam at 1550 nm.

3.2.3 Diffraction-limited 2 cm aperture

The 2.26 mrad beamwith of NODE (assumed to be used for FLARE) was selected on the basis of being as wide as possible while supporting a 10 Mbps link on a 10 W power budget[8], but narrower beams are achievable, such as the 15-microradian downlink beam used by LLCD.[7] A 100-microradian beam would require a diffraction-limited transmit telescope, with an aperture size of 2 cm, which is physically achievable in a CubeSat, but would challenge the two-stage pointing found to be necessary to enable the fine pointing that NODE requires. However, a dedicated gimbal assembly of the required accuracy could be supported by a 100-kg microsatellite. For example, the NFIRE-LCT had a pointing error of approximately 170 microradians[29] and a mass of 35 kg[30].

3.2.4 High-cost SHG FLARE

This case is identical to Diffraction-limited FLARE, with the exception that it assumes 3.6 W is required to use SHG. This is not expected to be realistic; rather, it is used to validate the model by producing poor performance at low electrical power budgets (where P_{shg} is of the same order of magnitude as P_{elec}).

3.2.5 Half-angle FLARE

Some of the improvement in link margin from SHG comes from the 6 dB increase in received power from reducing the beamwidth by a factor of 2. This case compares the stock FLARE to a link with a beamwidth of 1.13 mrad, to compare the improvement from SHG with the improvement that comes from simply reducing the beamwidth while staying at the same wavelength.

3.2.6 Diffraction-limited FLARE with GM-APDs

At ranges longer than 200 km (and 5.7 W of electrical power), the amount of photons-per-bit passes below 1,000, the original design goal of NODE, and distances beyond 350 km, it can pass below 200 photons-per-bit, the measured sensitivity of NODE's receiver design.[8] Under such conditions, avalanche photodiodes are no longer an appropriate technology; it is better to use direct photon-counting with Geiger-mode APDs. This case analyzes the bit rate capacity of the link with InGaAs and silicon GM-APDs. The slot width T_s was changed for this case, to accommodate the pulse length of the GM-APD output. The GM-APD's pulse length is 20 ns, so the slot width was set to 40 ns. The range limits were also changed. The maximum range was set to 1 million km (approximately the distance to the Earth-Sun L_1 or L_2 Lagrange points) to reach the SNR regime where the different noise characteristics of InGaAs and silicon become meaningful.

Chapter 4

System Design Results

4.1 FLARE

The first case run was the direct duplicate of FLARE/NODE, with the optical link parameters as shown in Table 2.1. A contour plot of the resulting differences in margins – in other words, the link margin at 775 nm (5.69 dB) minus the link margin at 1550 nm (6.77 dB) – is shown in Figure 4-1. At FLARE's current design point (5.7 W electrical, 200 km range), the improvement in margin is -0.86 dB.

For most of the design space studied, the link margin was reduced. The reason for the large region between the -1 and -1.2 dB contours (i.e. the reason that the contours do not continue indefinitely towards the right side of the graph) is that silicon gain tops out at 1000 (the maximum recommended by the datasheet[17])[1] and InGaAs gain tops out at 63.4. The optimum gains for the InGaAs and silicon APDs, when electrical power is held at 5.7 W, are shown in Figure 4-2 (with the InGaAs gain shown in more detail in Figure 4-3).

Note that, for crosslink ranges greater than approximately 500 km, the difference in gains between the two cases is approximately constant. At large gains, the noise factor $F_A \approx k_A M_{APD}$, per Equation 1.9. When gain and excess noise factor are constant with range, then so are σ_{on}^2 and σ_{off}^2 for both the 1550 and 775 nm cases, per

[1] In the extreme case, of 10,000 km and 5 W of electrical power, the receiver is seeing single photons-per-bit, and it would be better to operate Geiger-mode APDs and count photons. It was this observation that motivated case 6.

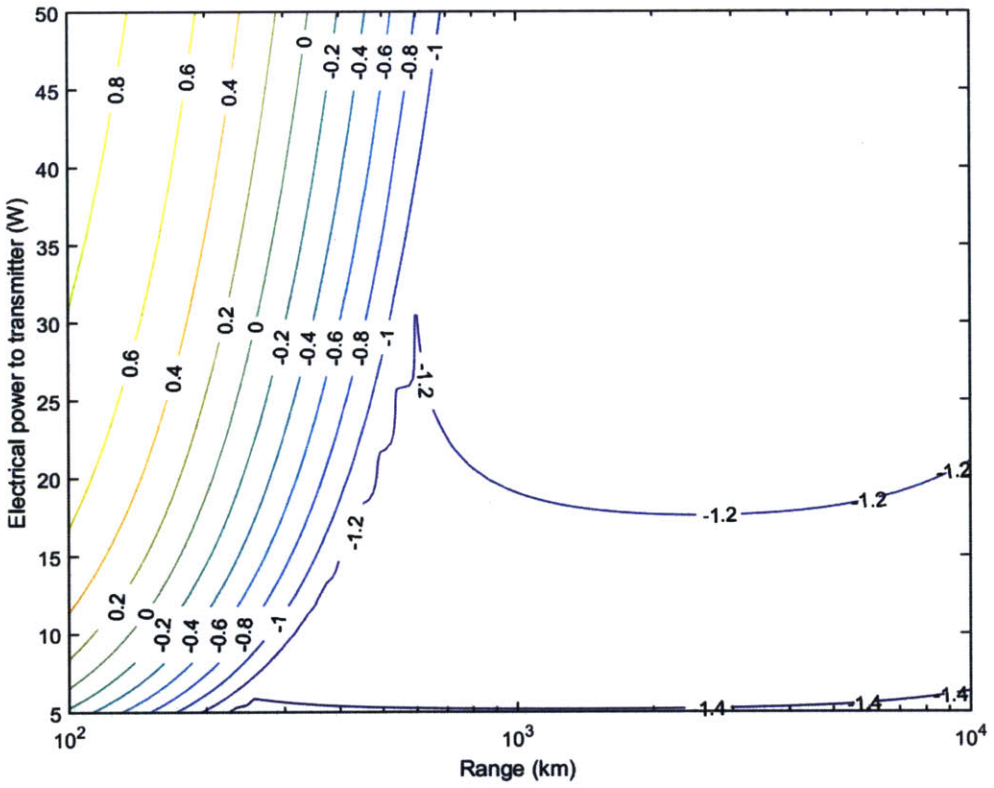

Figure 4-1: Improvement in FLARE's optical link-budget margin with collimation-limited optics and frequency-doubler (dB). The distortion of the -1.2 dB contour is a MATLAB artifact from the discrete test points and reduced rate of change.

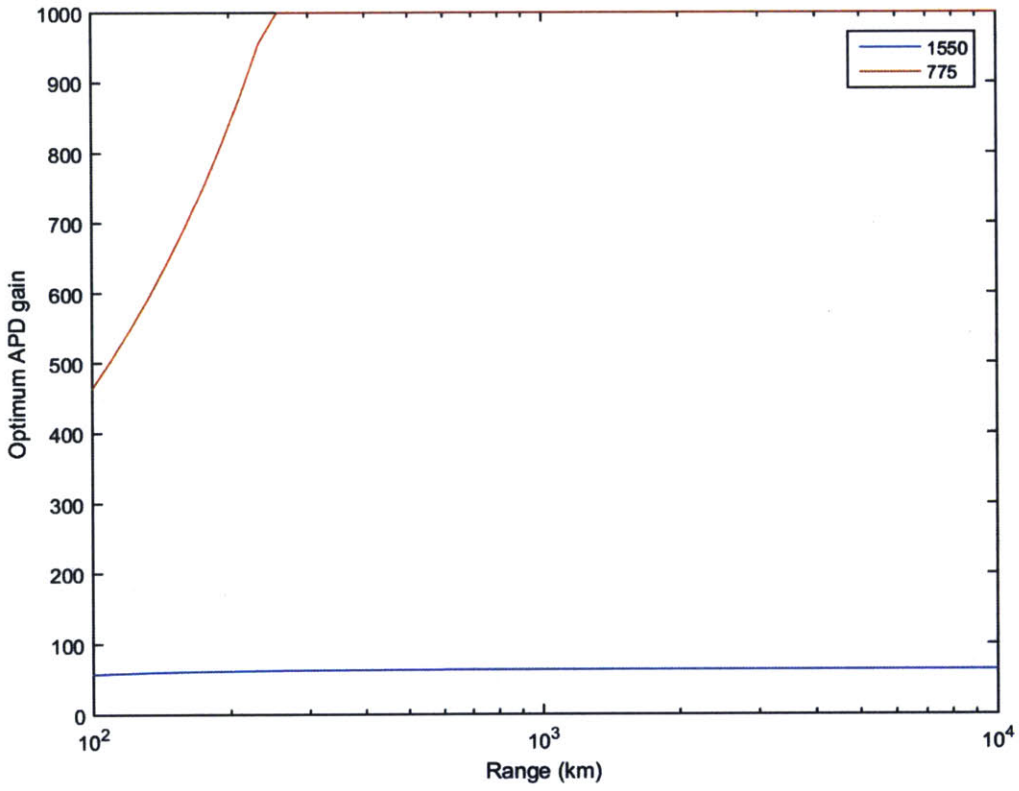

Figure 4-2: Optimum gain of silicon and InGaAs APDs, for FLARE case study (collimation-limited, 5.7 W electrical).

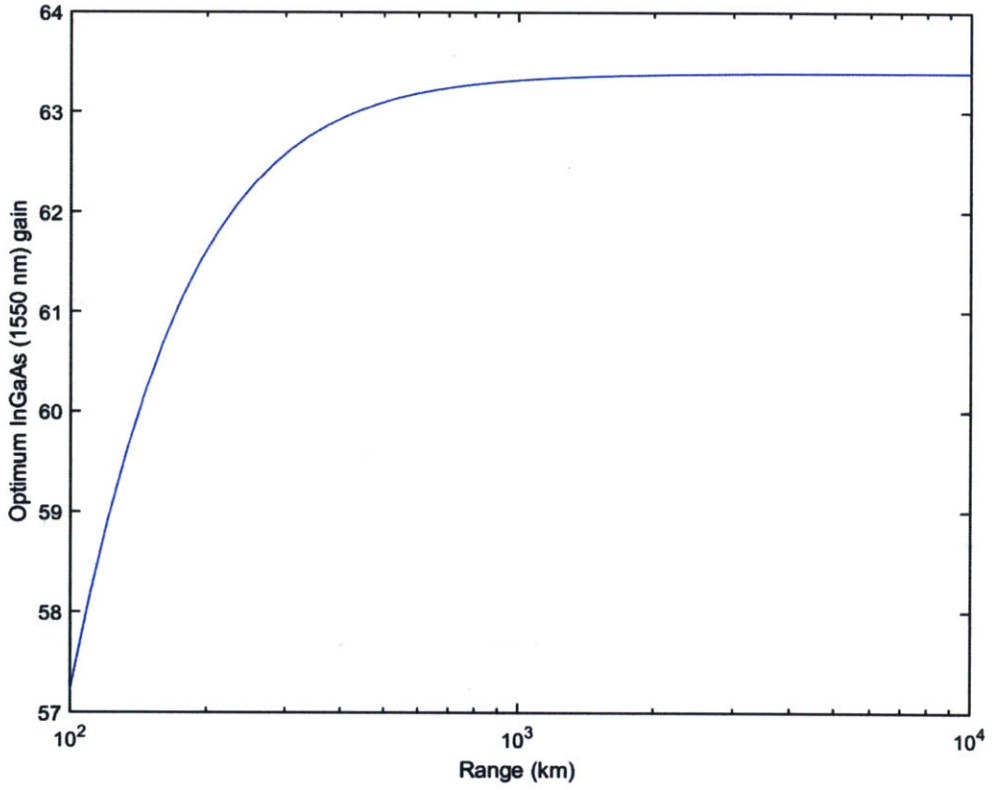

Figure 4-3: Optimum gain of InGaAs APD, for FLARE case study (collimation-limited, 5.7 W electrical).

Equation 2.9 and Equation 2.10. This implies a constant $\mu_{i,on,req}$ and thus P_{req}. While the link margins are changing (in particular, they decrease with distance, eventually becoming negative, as the power required stays the same but power received decreases with distance), they do so at the same rate for both the 1550 nm and 775 nm cases.

4.2 Diffraction-limited FLARE

This case is identical to the first, except that the collimator is replaced by a 1.67 mm aperture, to produce an identical beamwidth at 1550 nm, while allowing the 775 nm beam to be narrower.[2] A contour plot of the resulting differences in margins is shown in Figure 4-4. At FLARE's current design point (5.7 W electrical, 200 km range), the improvement in margin is 3.3 dB.

We are seeing the lower-bound on the link budget improvement from SHG identified in the first case. It is shifted to longer ranges, as the higher received power from the extra 6 dB of transmitter gain keeps the optimum silicon APD gain below 1000 for longer. However, we are also beginning to see that there is a maximum improvement as well. The maximum and its causes are more apparent in the diffraction-limited case with the 2 cm aperture.

4.3 Diffraction-limited 2 cm aperture

This case is identical to the second, except that the collimator is replaced by a 2 cm aperture, to produce a beamwidth of 189 microradians at 1550 nm, while allowing the 775 nm beam to be narrower. A contour plot of the resulting differences in margins is shown in Figure 4-5. At FLARE's current design point (5.7 W electrical, 200 km range), the improvement in margin is 4.3 dB.

This case shows a notable peak where FDOT is maximally effective, with a decrease in performance at closer and further distances. The cause is once again related to APD gains. The optimum gains for the InGaAs and silicon APDs, when electrical

[2]In practice, this would result in pointing losses becoming more severe when operating at 775 nm.

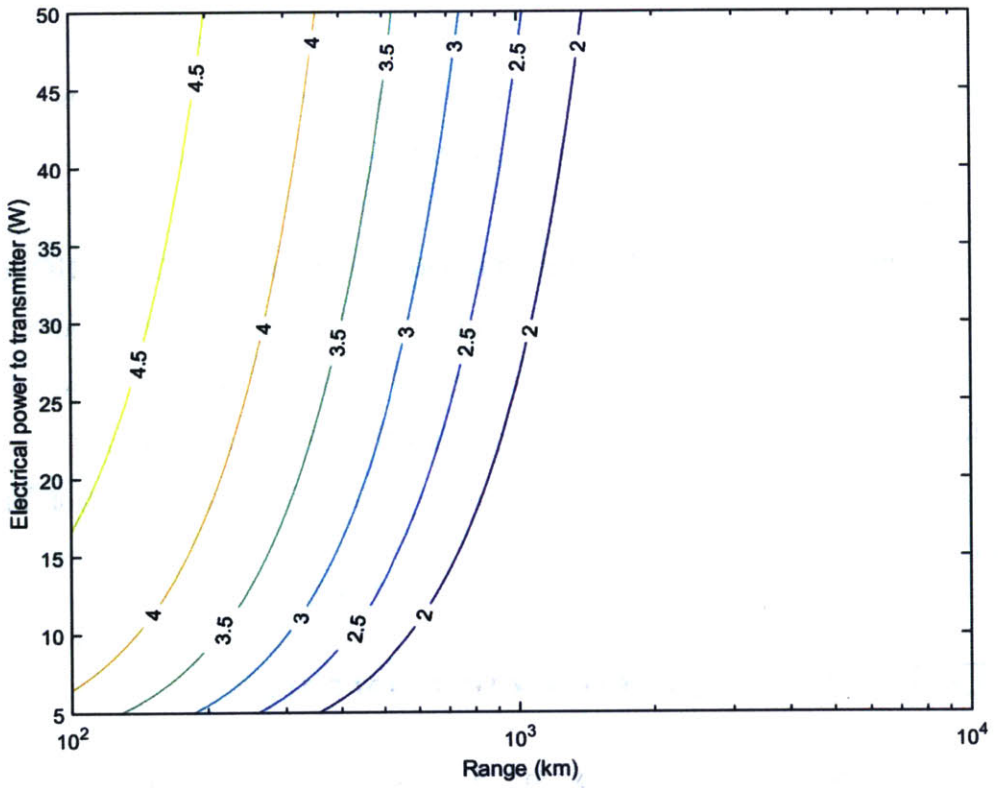

Figure 4-4: Improvement in FLARE's optical link-budget margin with frequency-doubler (dB), diffraction-limited case.

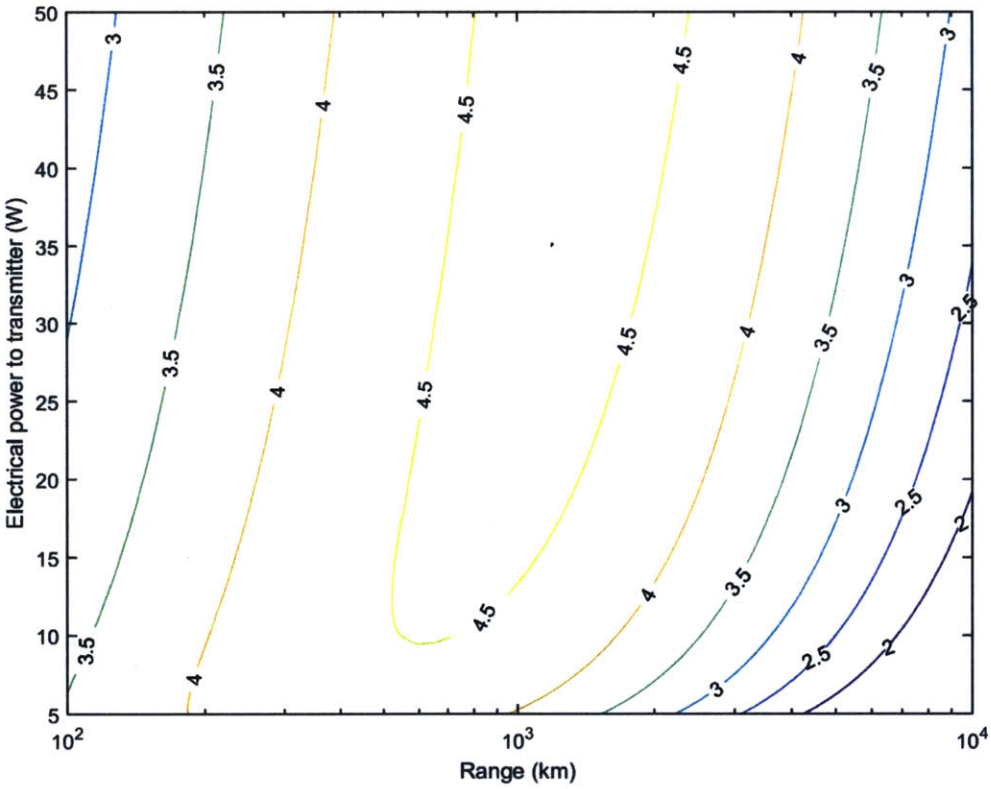

Figure 4-5: Improvement in 2 cm diffraction-limited optical link-budget margin with frequency-doubler (dB).

power is held at 5.7 W, are shown in Figure 4-6 (with the InGaAs APD shown alone in Figure 4-7).

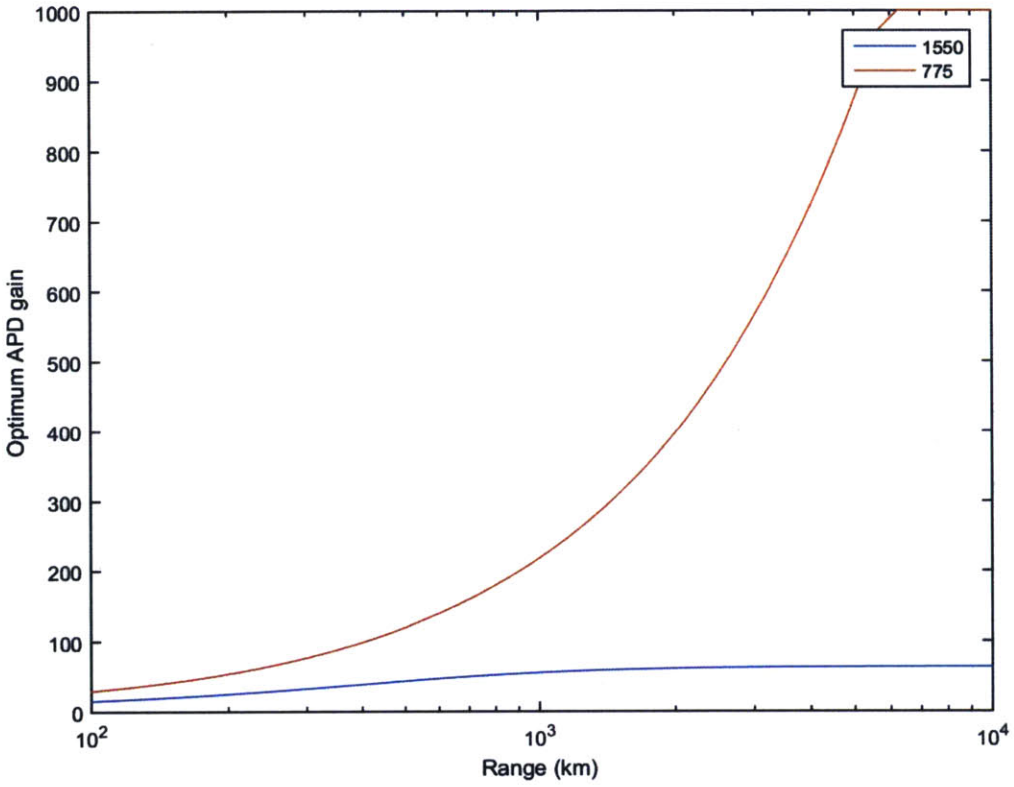

Figure 4-6: Optimum gain of silicon and InGaAs APDs, for 2 cm diffraction-limited case study.

We observe that the optimum gain for the silicon case decreases very slowly at ranges less than 1,000 km (where the link margin improvement starts to decrease again) while the InGaAs optimum gain decreases much more (proportionately). When gain is held constant or nearly so, the noise terms that influence Q (and thus the required power), σ_{on}^2 and σ_{off}^2 depend on the average photocurrents (i.e. shot noise), which increase as the range decreases. For 5.7 W operating power, σ_{on}^2 is plotted in Figure 4-8. In particular, note that as the range closes to 1,000 km, σ_{on}^2 is decreasing in the 775 nm case (except for the very furthest ranges, where the gain tops out and hampers link margin improvement) and increasing in the 1550 case, while the behavior reverses as the range continues to close.

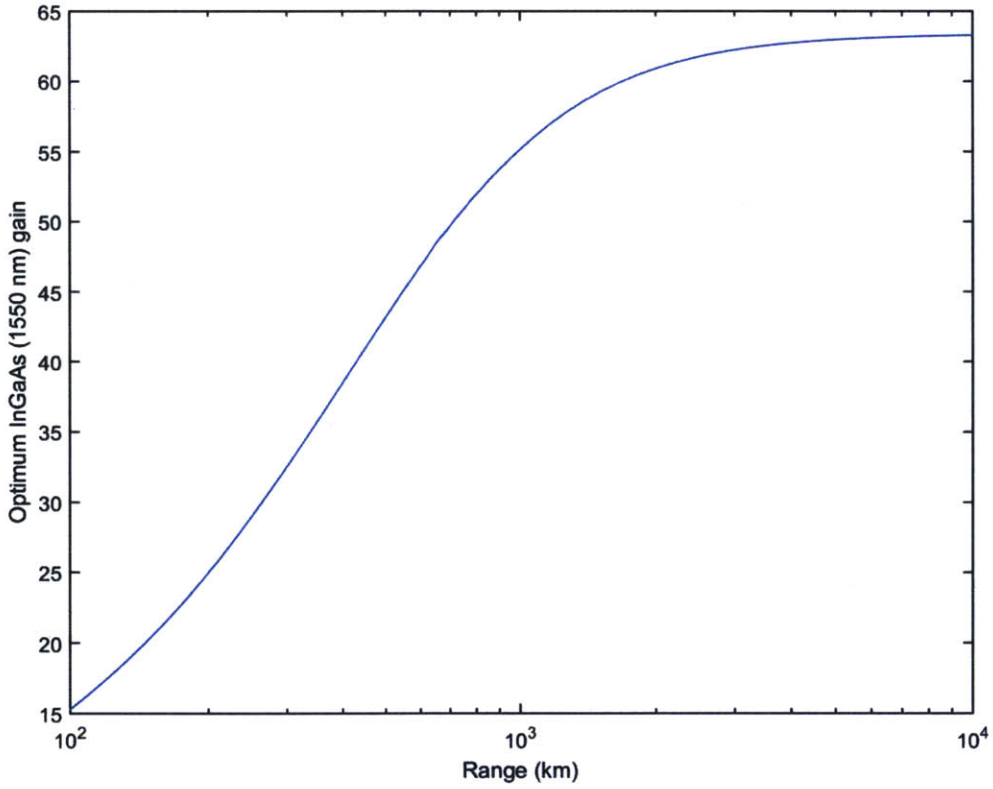

Figure 4-7: Optimum gain of InGaAs APD, for 2 cm diffraction-limited case study.

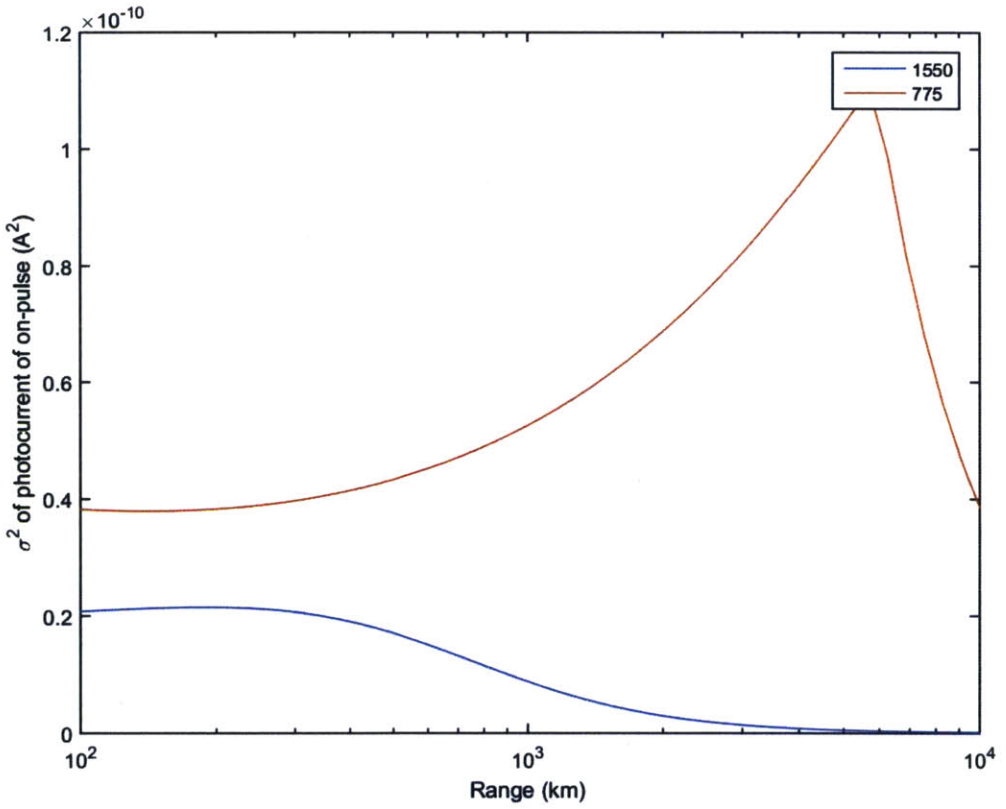

Figure 4-8: σ_{on}^2, for 2 cm diffraction-limited case study.

4.4 High-cost SHG FLARE

This case (collimator-limited, like the original FLARE) was not considered to be representative of a desirable design, but to validate the model – to show losses at low electrical power, where 3.6 W cannot be spared. A contour plot of the resulting differences in margins is shown in Figure 4-9. At FLARE's current design point (5.7 W electrical, 200 km range), the improvement in margin is -3.3 dB.

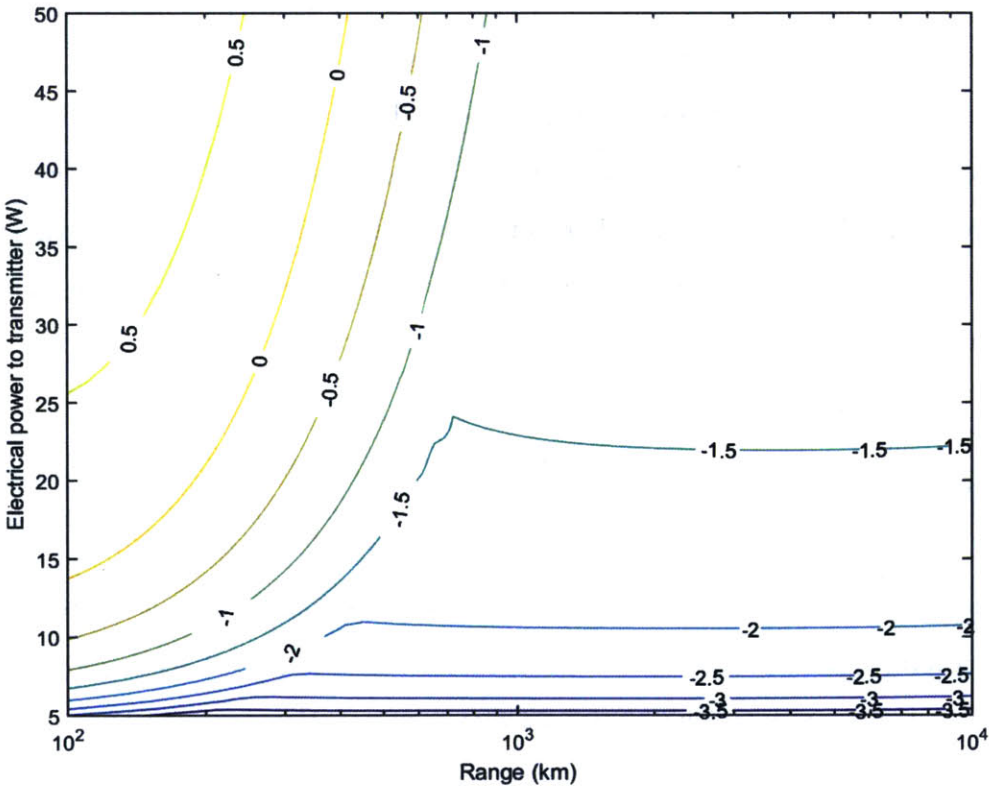

Figure 4-9: Improvement in FLARE optical link-budget margin with high-power-cost frequency-doubler (dB).

The impact on link margin at low power costs is as expected: reducing the power budget from 5.7 W by 3.6 W is the equivalent of -4.3 dB. The reduction in incoming power allows the APD's optimum gain to rise from 800 to 1000 (+1 dB, although the relationship from APD gain to link margin is not linear), which partly compensates for the power loss.

4.5 Sensitivity

SHG is sensitive to temperature and polarization; from Figure 1-5, we can see that being off-center by 3 K can result in reductions in conversion efficiency of more than 10%. Conversely, while the experiment by Bill Farr and the author measured a maximum conversion efficiency of 75% (the figure used throughout these case studies), efficiencies of up to 85% have been measured (with KTP doubling 1060 nm, rather than PPLN)[43]. The sensitivity of the link-budget improvement in diffraction-limited FLARE to variations in SHG conversion efficiency is plotted in Figure 4-10. From this, we can conclude that the effect of ±0.6 dB changes in efficiency produces ±0.4 dB changes in the difference in link margins from FDOT. This analysis and Figure 1-5 imply that, in order to keep the link margin improvement above 3 dB, conversion efficiency must be kept above 74%, which would require the crystal in Farr's experiment to be held within ± 1 degree K of its optimum operating point, although crystals with better peak efficiencies may have more leeway.

4.6 Model validity

In addition to the impact of the electrical power requirement at low system power budgets, there appear to be two limiting factors: the limits of APD gain at long ranges, and the growth of shot noise at close range. However, APDs themselves may not be the appropriate receiver technology to use in those circumstances. To judge the validity of the model in those regimes, plots are made of difference in link margin versus the photons-per-bit (using the diffraction-limited FLARE case, as that exhibited a higher increase in link margin than FLARE itself did) in Figure 4-11 and of the actual link margin (at 1550 nm) vs. photons-per-bit in Figure 4-12.

NODE's design goal was to have 1,000 photons received per bit, to simplify receiver design, although the link could be closed with as few as 125 (i.e. 21 "dB-ppb")[8, Fig. 4-15]. This means that, while it is true that the improvement in link margin "freezes" at long ranges when gain cannot be increased, the link margin itself is negative and

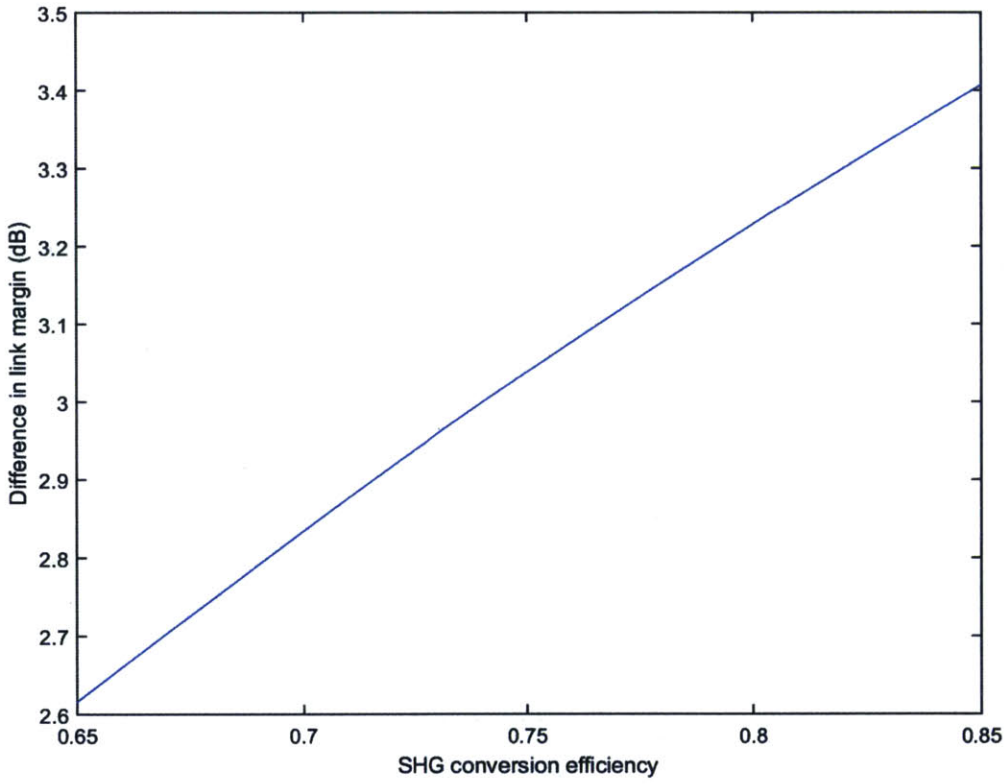

Figure 4-10: Link margin improvement from FDOT vs. SHG efficiency for diffraction-limited FLARE (5.7 W, 200 km).

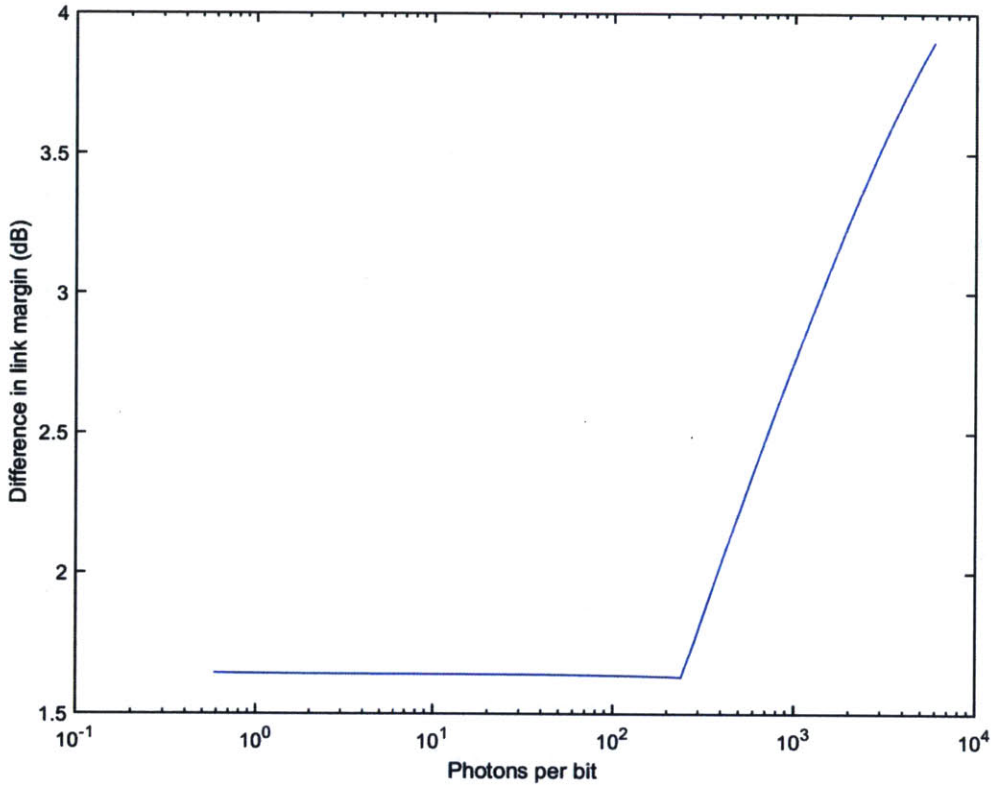

Figure 4-11: Change in margin by FDOT vs. received-photons-per-bit (at 1550 nm), for diffraction-limited FLARE case study at 5.7 W, 200 km.

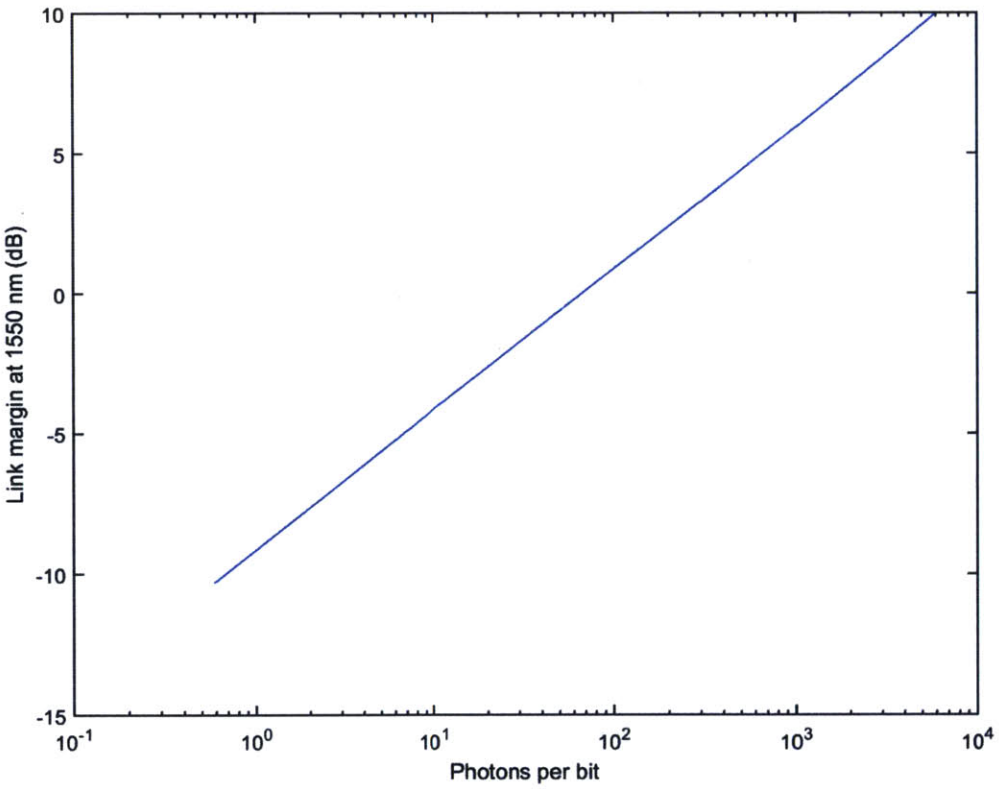

Figure 4-12: Link margin at 1550 nm vs. received-photons-per-bit, for diffraction-limited FLARE case study.

APDs are not appropriate to apply there. It would be better to apply Geiger-mode APDs, which have been successfully operated at fewer than 1.5 ppb[20], and for which the concept of "gain" does not apply, as they are intentionally biased beyond the breakdown voltage to produce an avalanche of electrons at the incidence of a single photon. This observation motivated the final case: to replace the linear-mode APDs with geiger-mode APDs.

When the link budget improvement starts to decrease at close ranges, it is clear that link margins and photons-per-bit count are so high that there is no need for a few dB of improvement from FDOT. There is ample margin to increase data rate, reduce transmit power, or expand the beam to ease pointing requirements.

From this, we can conclude that, if a laser system is "well-suited" for APDs in linear mode, with several hundred to a few thousand photons per bit, the link budget can be improved by 3-4 dB by using FDOT. However, this assumes that the system's pointing loss is no worse in the 775 nm case – in other words, that the system can adequately point a beam with half the beamwidth of the 1550 nm beam. This observation motivated the next case: to evaluate the impact of simply narrowing the 1550 nm beamwidth itself, without incorporating a frequency-doubling nonlinear optical element.

4.7 Half-angle FLARE

This case compares the improvement from SHG with the improvement that comes from simply reducing the beamwidth while staying at the same wavelength. A contour plot of the resulting differences in margins is shown in Figure 4-13. At FLARE's current design point (5.7 W electrical, 200 km range), the improvement in margin is 3.3 dB.

At long ranges, where APD gain is maximized and constant in both cases, the 6 dB improvement is reduced by the dependency of shot noise on the square root of received power. At close ranges, the received power is high enough that the APD gain can be reduced, which reduces shot noise relative to the amount of power received

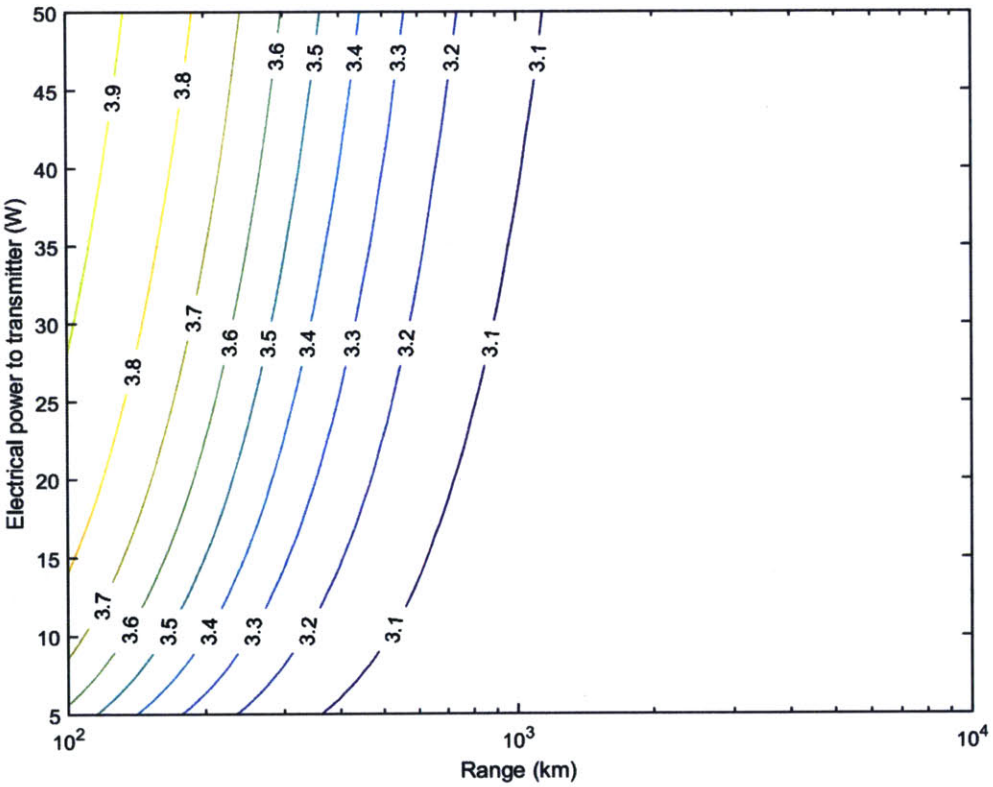

Figure 4-13: Improvement in collimator-limited FLARE optical link-budget margin by halving the beamwidth (dB).

and further improves SNR and the link margin improvement.

4.8 Diffraction-limited FLARE with Geiger-mode APDs

For this case, the assumption that channel capacity is limited by modulation is no longer valid. Rather than calculating the link margin, this case evaluates the channel capacity directly by combining the GM-APD SNR equation (Equation 1.10) and the channel capacity equation (Equation 2.1). The channel capacities for FLARE (collimator-limited, 5.7 W of electrical power) are shown in Figure 4-14. At 200 km, the improvement in capacity is 1.5×10^{-5} dB.

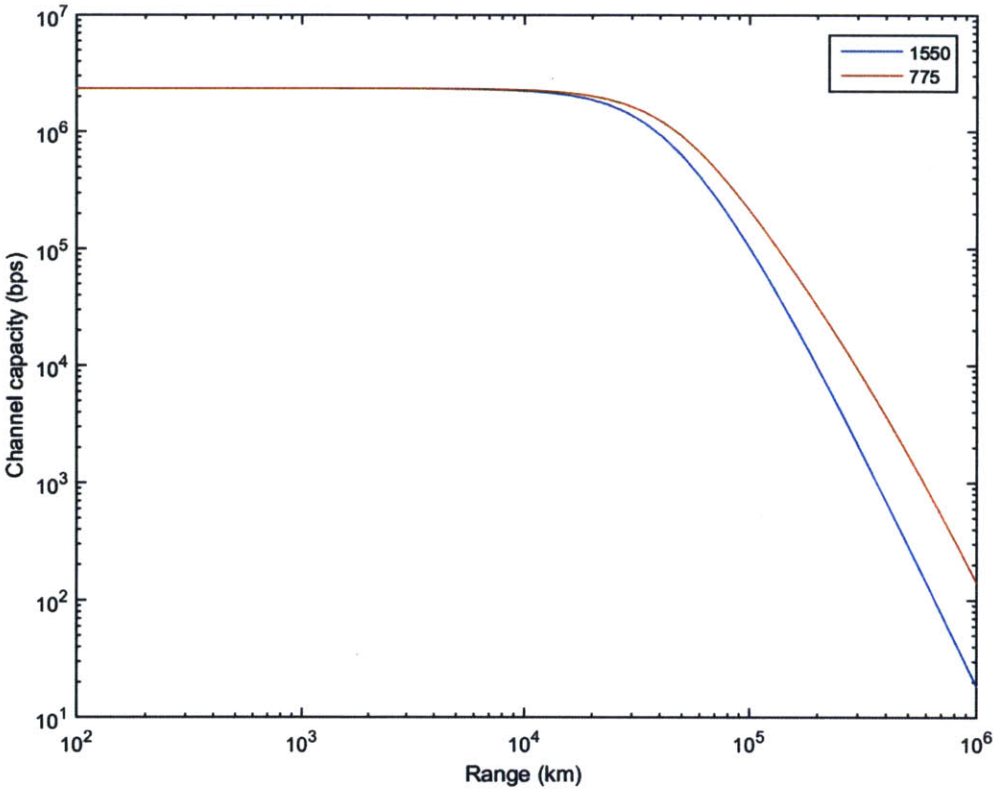

Figure 4-14: Channel capacity in diffraction-limited FLARE with frequency-doubling, when received by Geiger-mode APDs.

At ranges up to 10,000 km (i.e. LEO links), the SNR is such that the link capacity is limited by the modulation of the laser, even at fewer than 10 photons-per-bit.

However, as the link range gets longer and SNR falls, the link enters the regime identified by Moision and Farr[6] where noise power dominates and the channel capacity depends on $1/R^4$ (note that the channel capacity falls by 2 orders of magnitude for the 1550 nm case between 100,000 km and 1 million km). However, because of the reduced dark count of the silicon APDs, the transition occurs later in the silicon case, and so the capacity is nearly an order of magnitude better (9-10 dB).

Chapter 5

Science Applications of Frequency-Doubling Nonlinear Optics

We have seen that frequency-doubling nonlinear optics can improve crosslink budgets, but not by much more than other, simpler design modifications. In this chapter, the utility of nonlinear optics in laser communication systems for science applications is evaluated.

5.1 Satellite-mounted light source

Another potential application of FDOT is to allow an infrared communication laser to behave as a visible light source for photometric calibration of telescopes. This has been demonstrated at 532 nm from the CALIPSO satellite, and is desired at more wavelengths for better science returns.[38] Per [38, Eq. 2], the apparent magnitude of an orbiting laser imaged by a ground-based telescope is:

$$m \approx -2.5 \log_{10} \left(\frac{P}{h^2 d^2} \right) - 20.1 \tag{5.1}$$

Where P is laser power in milliwatts, h is the height of the orbit in kilometers, and d is the divergence of the laser beam in milliradians.

A table of the apparent magnitudes at 775 nm of each case is given in Table 5.1.

Table 5.1: Apparent magnitude of 775 nm beam for various cases.

Operating case	Apparent magnitude
FLARE, collimator-limited	-11.5
FLARE, diffraction-limited	-13.0
2-cm, diffraction-limited	-18.4
FLARE, high-SHG-cost	-11.2

This is easily bright enough to be imaged in a telescope. Individual passes are brief, on the order of ten minutes, and unlikely to be in the direction desired by a particular astronomer at a particular time; however, nanosatellites are inexpensive enough to be assembled and launched in quantities large enough to increase the probability of useful passes, so a fleet of nanosatellites bearing FDOTs could be used not only for global communication but also for astronomical purposes. There is also ample margin to deploy a smaller number of satellites in higher orbits to improve visibility time and reduce the slew rate.

5.2 Difference Frequency Generation for atmospheric science

Difference Frequency Generation (DFG) is a second-order nonlinear process, like second-harmonic generation, but rather than producing light at twice the frequency of the input, the output is two waves at frequencies which sum to the input frequency (or, in the degenerate case, one wave at half the frequency). To achieve high conversion efficiencies (20-30%[44], rather than 75% or more for SHG), the input light must be passed through the crystal multiple times, often by means of a resonator cavity, in an Optical Parametric Oscillator (OPO). This is considerably more complicated than the setup required for SHG, but it has the advantage of being very broadly tunable. Experimental OPO demonstrations have produced output light from 420 through 2300 nm from a single 355 nm pump source[44], and modern (and larger) benchtop OPOs can tune to 4000 nm.[45] These wavelengths are useful for probing

atmospheric composition.[37]

Because the purpose of a frequency-*differencing* optical transmitter ("FDiOT") would be for science rather than communication, there is no need for the high modulation speeds that led Ryan Kingsbury to choose the MOPA configuration over High-Power Laser Diode (HPLD) for NODE, so that is the architecture that FDiOT is competing against. Kingsbury found experimentally that, with temperature and current tuning, a laser diode's wavelength can be varied by approximately 2 nm[8, Fig. 4-4][1], which means that over 900 laser diodes would be required to match the dynamic range that a single OPO can achieve, which would have a mass of over 90 kg. While most OPOs in use are benchtop laboratory models, not optimized or certified for space applications, they certainly have lower masses than 90 kg, and the volume of the OPO made by Bosenberg *et al.* is compatible with the capacity of a 6U CubeSat (55 mm in length)[44]. The German Aerospace Center (DLR) has investigated and developed an OPO intended for airborne and spaceborne atmospheric composition investigations, although it is intended for larger aircraft and spacecraft platforms.[46]

DFG and four-wave mixing (another nonlinear optical process) can also be exploited to generate frequency combs. Two lasers of slightly different wavelengths are pumped through highly nonlinear fiber, and the resulting nonlinear interactions produce finely-spaced peaks in the frequency domain. For example, J.M. Chavez Boggio *et al.* (UCSD) demonstrated an optical comb generated from lasers operating at 1550 and 1550.8 nm, producing a frequency comb that extended from 1400 to 1750 nm, with a channel spacing of 100 GHz (0.8 nm). That experimental setup included two EDFAs and several meters of fiber, which is greater than the volume budget of NODE's initial demonstration can sustain, but could be contained in a CubeSat. The total bandwidth of the frequency comb is less than that achievable by an OPO, but many more wavelengths are produced simultaneously. The comb can then be used to probe the atmosphere at the mid-infrared wavelengths.

[1]Note that the TEC can operate the laser at up to 40 C.

Chapter 6

Conclusion

We have analyzed the effects of a frequency-doubling nonlinear optical element on FLARE, a planned nanosatellite experiment to demonstrate an intersatellite crosslink in LEO. With the system as-designed, the link margin is improved by 0.09 dB, which may easily be lost in implementation. However, when applied with a diffraction-limited system, the link margin can be improved by 3-4 dB, provided that the system is operating in a regime where APDs are sensible to use (i.e. approximately 1000 photons per bit). A similar improvement can be obtained more simply, by narrowing the beamwidth of the 1550 nm laser by a factor of 2. However, for links at longer ranges (beyond LEO), where photon-counting Geiger-mode APDs are required, the improvement offered by SHG can be as much as 10 dB.

6.1 Contributions

Two design tools were developed. The first is an extension of a link-budget analysis tool currently used at MIT[1] to study link budgets where the detector is a linear-mode APD, and the goal is to obtain the link margin above the power required to statistically distinguish PPM pulses at a desired data rate. The second calculates the channel capacity of an optical link where the detector is a Geiger-mode photon-

[1]Developed by Ryan Kingsbury for NODE[8], extended by Emily Clements for uncertainty analysis of NODE's link budget[27], and then by the author to incorporate SHG and different detector types.

counting APD. This technology is not expected to be used for any MIT CubeSat missions at this time, but has been used in MIT Lincoln Lab's Lunar Laser Communication Demonstration[7].

6.2 Future Work

While FDOT's improvement to a link budget may not be enough to motivate its development for currently-planned LEO missions, it may be beneficial for a satellite guidestar mission. This application will be studied in more detail. Other nonlinear optical processes, such as difference-frequency generation, may be applied to allow communications lasers to also generate longer wavelengths suitable for atmospheric science. A frequency-*differencing* optical transmitter will be developed to allow CubeSats to contribute to atmospheric spectroscopy with their laser communication payloads.

Appendix A

Code

The code of the analysis in this thesis is built up in nested functions.

A.1 Linear-mode Link Margin

The `linkmargin` function calculates the margin of a PPM link where the detector is an APD operated in linear mode. It takes 21 variables as arguments, which would be impractical to set for every case. To simplify case generation, there is a wrapper function called `basecase`, which sets several variables which are common to all cases analyzed (e.g. receiver diameter, PPM order, and slot width). `basecase` is in turn wrapped by `base_1550` and `base_775`, which define variables common to all 1550 nm and 775 nm cases, respectively (wavelength, APD quantum efficiency, dark current, and the variables k_A and x which feed the excess noise and optimum gain equations), leaving only the transmitted optical power, beamwidth, range, and sky radiance to be set for each case.

A.1.1 linkmargin

```
function [Prx,appmag,phot_per_bit,Mopt,margin,mu_i_on,sigma2_on] =
    linkmargin(Ptx,BW,range,PPM,ER,Ts,BER,lambda,L_sky,Drx,D_sens,
    foclen,Lrx,qeff,Id,T,kA,x,Fn,RL,Limp)

c = 299792458; % speed of light
q = 1.60218e-19; % charge on the electron
kB = 1.38065e-23; % boltzmann
h = 6.626e-34; % Planck

spaceloss = (lambda./(4.*pi.*range)).^2;

Grx = (pi.*Drx./lambda).^2;

Gtx = 2/(1 - cos(BW./2));

Prx = Ptx.*Gtx.*spaceloss.*Grx.*10.^(Lrx./10);

appmag = -2.5.*log10(Ptx.*1000./(range.*BW).^2) - 20.1;

nu = c./lambda;

Resp = qeff.*q./(h.*nu);

bitrate = log(PPM)/(log(2)*PPM*Ts);

phot_per_bit = Prx./(h*nu.*bitrate);

Arx = pi*(Drx/2)^2;

FOV = D_sens/foclen;

FOVsa = 2*pi*(1-cos(FOV/2));

Pbckg = Arx.*FOVsa.*L_sky.*10.^(Lrx./10);
```

```
33
Mopt = min((4.*kB.*T./(x.*q.*RL.*(Resp.*Prx + Id))).^(1/(2+x)),1000)
    ;
35
PRpkav = 1/((1/PPM) + (1-1/PPM)/ER);
37
PRoffav = 1/(1/(PPM/ER) + 1 - 1/PPM);
39
mu_i_on = Mopt.*Resp.*Prx.*PRpkav; % Photocurrent -- to capture the
    true "signal" seen by the detector
41
NEB = 1.5./Ts; % 1.5x slotrate, extrapolated from Kingsbury (300 MHz
     for 200 MHz slot clock)
43
FA = kA.*Mopt + (1 - kA).*(2-1./Mopt);
45
NEP = sqrt(4.*kB.*T.*Fn./(RL.*Resp.^2));
47
sigma2_amp = (NEP.*Resp.*Mopt).^2;
49
sigma2_on = 2*q.*Resp.*(Mopt.^2).*NEB.*FA.*(Pbckg + Prx.*PRpkav) +
    sigma2_amp;
51
sigma2_off = 2*q.*Resp.*(Mopt.^2).*NEB.*FA.*(Pbckg + Prx.*PRoffav) +
     sigma2_amp;
53
mu_i_off = Resp.*Mopt.*(Pbckg + Prx.*PRoffav);
55
Q = sqrt(2).*erfcinv(4.*BER./PPM);
57
mu_i_onreq = Q.*sqrt(sigma2_on + sigma2_off) - mu_i_off;
59
Psig = (mu_i_onreq./(Mopt.*Resp) - Pbckg)./(PRpkav);
61
Preq_db = 10.*log10(Psig) - Limp;
63
```

```
Prec_db = 10.*log10(Prx);

margin = Prec_db - Preq_db;
end
```

A.1.2 basecase

```
% Base case -- setting up the variables common to all runs.

function [Prx,appmag,phot_per_bit,Mopt,margin,mu_i_on,sigma2_on] =
    basecase(Ptx,BW,range,lambda,L_sky,qeff,Id,kA,x)

Fn = 4.3; % "next"-stage amplifier noise factor, measured by
    Kingsbury/NODE
RL = 50; % Standard load, typ value per Hamamastu
Ts = 1/2e8; % Per Kingsbury/NODE
Drx = 0.085; % 85 mm aperture, from FLARE proposal
BER = 1e-4; % Capable of being handled with coding.
PPM = 64; % Per Kingsbury/NODE
ER = 10^(42/10); % 42 dB, per Clements
Limp = 4; % 4 dB of implementation losses, per Clements -- postive
    for loss, opposite convention of Lrx and Ltx
Lrx = 0; % Assume no optical loss in the detector.
T = 298; %Standard room temperature -- a nanosat can easily keep the
     APD at this temperature.
D_sens = 200e-6; % 200 um sensor active area
foclen = 1.8.*Drx; % f/1.8 lens

[Prx,appmag,phot_per_bit,Mopt,margin,mu_i_on,sigma2_on] = linkmargin
    (Ptx,BW,range,PPM,ER,Ts,BER,lambda,L_sky,Drx,D_sens,foclen,Lrx,
    qeff,Id,T,kA,x,Fn,RL,Limp);

end
```

A.1.3 base_1550

```
function [Prx,appmag,phot_per_bit,Mopt,margin,mu_i_on,sigma2_on] =
    base_1550(Ptx,BW,range,L_sky)

lambda = 1550e-9;

qeff = 0.72; % Per Hamamatsu, G8931-04
Id = 40e-9;

kA = 0.45; % Per Excelitas
x = 0.7;

[Prx,appmag,phot_per_bit,Mopt,margin,mu_i_on,sigma2_on] = basecase(
    Ptx,BW,range,lambda,L_sky,qeff,Id,kA,x);

end
```

A.1.4 base_775

```
function [Prx,appmag,phot_per_bit,Mopt,margin,mu_i_on,sigma2_on] =
    base_775(Ptx,BW,range,L_sky)

lambda = 775e-9;

qeff = 0.85; % Per Hamamatsu, S12023-10
Id = 30e-12; % Per Ham, but not found for S12023 specifically.

kA = 0.02; % Per Excelitas, general-purpose "reach-through"
    structure
x = 0.3;

[Prx,appmag,phot_per_bit,Mopt,margin,mu_i_on,sigma2_on] = basecase(
    Ptx,BW,range,lambda,L_sky,qeff,Id,kA,x);
end
```

A.1.5 Case 1: FLARE

```
%%Case 1: FLARE

close all;
%%

elec_pwr_vec = linspace(5,50); % Electrical power to transmitter,
    Watts
range_vec = logspace(5,7); % Range, 10^x meters


Ltx = -3; % For polarization-switching

Lsky = 0; % Space-to-space link, no atmospheric noise

shg_pwr = 0.62; % For a 3.3V polarization switcher at 50 ohm -> 0.22
     watts, plus 0.4 W for TEC.

edfa_eff = 0.035; % based on Ryan's thesis -- 200 mW optical from
    5.7 W electrical.

shg_eff = 0.75; % 0.75 based on experiment w/ Bill at JPL -- could
    be as much as 84% according to ThorLabs ads.

BW = 2.26e-3;

elec_pwr = 5.7; % NODE: 5.7 W -> 200 mW laser power
range = 200000; % FLARE: 200 km

pt_1550 = elec_pwr.*edfa_eff.*10^(Ltx/10);
pt_775 = (elec_pwr - shg_pwr).*edfa_eff.*shg_eff.*10^(Ltx/10);

[~,~,~,~,marg_1550,~,~] = base_1550(pt_1550,BW,range,Lsky);
[~,appmag,~,~,marg_775,~,~] = base_775(pt_775,BW,range,Lsky);
```

```
marg_diff = marg_775 - marg_1550;

display(marg_775)
display(marg_1550)
display(marg_diff)
display(appmag)

%%
[elec_pwr,range] = ndgrid(elec_pwr_vec,range_vec);

pt_1550 = elec_pwr.*edfa_eff.*10^(Ltx/10);
pt_775 = (elec_pwr - shg_pwr).*edfa_eff.*shg_eff.*10^(Ltx/10);

[~,~,~,~,marg_1550,~,~] = base_1550(pt_1550,BW,range,Lsky);
[~,~,~,~,marg_775,~,~] = base_775(pt_775,BW,range,Lsky);
marg_diff = marg_775 - marg_1550;

%%

figure1 = figure;

contour(range./1000,elec_pwr,marg_diff,'ShowText','on');
xlabel('Range (km)')
ylabel('Electrical power to transmitter (W)')
set(gca,'xscale','log')

saveas(figure1,'C:\Users\Jimmy\Documents\MIT\Graduate Research\MS
    Thesis Template\Sec4figs\link-budget-improvement-flare.png')

%%

elec_pwr = 5.7;
range = logspace(5,7);

pt_1550 = elec_pwr.*edfa_eff.*10^(Ltx/10);
```

```
pt_775 = (elec_pwr - shg_pwr).*edfa_eff.*shg_eff.*10^(Ltx/10);

[~,~,~,Mopt_1550,marg_1550,~,~] = base_1550(pt_1550,BW,range,Lsky);
[~,~,~,Mopt_775,marg_775,~,~] = base_775(pt_775,BW,range,Lsky);
marg_diff = marg_775 - marg_1550;

%%

figure2 = figure;
plot(range./1000,Mopt_1550)
set(gca,'xscale','log')
xlabel('Range (km)')
ylabel('Optimum InGaAs (1550 nm) gain')

figure3 = figure;
plot(range./1000,Mopt_775)
set(gca,'xscale','log')
xlabel('Range (km)')
ylabel('Optimum Silicon (775 nm) gain')

figure4 = figure;
plot(range./1000,Mopt_1550,range./1000,Mopt_775)
legend('1550','775')
set(gca,'xscale','log')
%set(gca,'yscale','log')
xlabel('Range (km)')
ylabel('Optimum APD gain')

saveas(figure2,'C:\Users\Jimmy\Documents\MIT\Graduate Research\MS
    Thesis Template\Sec4figs\optimum-ingaas-gain-flare.png')
saveas(figure3,'C:\Users\Jimmy\Documents\MIT\Graduate Research\MS
    Thesis Template\Sec4figs\optimum-silicon-gain-flare.png')
saveas(figure4,'C:\Users\Jimmy\Documents\MIT\Graduate Research\MS
    Thesis Template\Sec4figs\optimum-apd-gain-flare.png')
```

A.1.6 Case 2: Diffraction-limited FLARE

```
%% Case 2: Diffraction-limited FLARE

close all;
%%

elec_pwr_vec = linspace(5,50); % Electrical power to transmitter,
    Watts
range_vec = logspace(5,7); % Range, 10^x meters




Ltx = -3; % For polarization-switching

Lsky = 0; % Space-to-space link, no atmospheric noise

shg_pwr = 0.62; % For a 3.3V polarization switcher at 50 ohm -> 0.22
     watts, plus 0.4 W for TEC.

edfa_eff = 0.035; % based on Ryan's thesis -- 200 mW optical from
    5.7 W electrical.

shg_eff = 0.75; % 0.75 based on experiment w/ Bill at JPL -- could
    be as much as 84% according to ThorLabs ads.

Dtx =  0.00167345; %Equivalent to get the same BW as NODE in a
    diffraction-limited system

lambda_1550 = 1.55e-6;
lambda_775 = 775e-9;

theta_1550 = 2*1.22*lambda_1550/Dtx;
theta_775 = 2*1.22*lambda_775/Dtx;

elec_pwr = 5.7; % NODE: 5.7 W -> 200 mW laser power
```

```
range = 200000; % FLARE: 200 km

pt_1550 = elec_pwr.*edfa_eff.*10^(Ltx/10);
pt_775 = (elec_pwr - shg_pwr).*edfa_eff.*shg_eff.*10^(Ltx/10);

[~,~,~,~,marg_1550,~,~] = base_1550(pt_1550,theta_1550,range,Lsky);
[~,appmag,~,~,marg_775,~,~] = base_775(pt_775,theta_775,range,Lsky);

marg_diff = marg_775 - marg_1550;

display(marg_diff)
display(appmag)

%%
[elec_pwr,range] = ndgrid(elec_pwr_vec,range_vec);

pt_1550 = elec_pwr.*edfa_eff.*10^(Ltx/10);
pt_775 = (elec_pwr - shg_pwr).*edfa_eff.*shg_eff.*10^(Ltx/10);

[~,~,~,~,marg_1550,~,~] = base_1550(pt_1550,theta_1550,range,Lsky);
[~,~,~,~,marg_775,~,~] = base_775(pt_775,theta_775,range,Lsky);
marg_diff = marg_775 - marg_1550;

%%

figure1 = figure;

contour(range./1000,elec_pwr,marg_diff,'ShowText','on');
xlabel('Range (km)')
ylabel('Electrical power to transmitter (W)')
set(gca,'xscale','log')

saveas(figure1,'C:\Users\Jimmy\Documents\MIT\Graduate Research\MS
    Thesis Template\Sec4figs\link-budget-improvement-flarediff.png')

%%
```

```
elec_pwr = 5.7;
range = logspace(5,7);

pt_1550 = elec_pwr.*edfa_eff.*10^(Ltx/10);
pt_775 = (elec_pwr - shg_pwr).*edfa_eff.*shg_eff.*10^(Ltx/10);

[~,~,phot_per_bit_1550,~,marg_1550,~,~] = base_1550(pt_1550,
    theta_1550,range,Lsky);
[~,~,~,~,marg_775,~,~] = base_775(pt_775,theta_775,range,Lsky);

marg_diff = marg_775 - marg_1550;

figure2 = figure;
plot(phot_per_bit_1550,marg_diff)
%legend('1550','775')
set(gca,'xscale','log')
%set(gca,'yscale','log')
xlabel('Photons per bit')
ylabel('Difference in link margin (dB)')

figure3 = figure;
plot(phot_per_bit_1550,marg_1550)
%legend('1550','775')
set(gca,'xscale','log')
%set(gca,'yscale','log')
xlabel('Photons per bit')
ylabel('Link margin at 1550 nm (dB)')


saveas(figure2,'C:\Users\Jimmy\Documents\MIT\Graduate Research\MS
    Thesis Template\Sec4figs\margdiff-vs-ppb.png')
saveas(figure3,'C:\Users\Jimmy\Documents\MIT\Graduate Research\MS
    Thesis Template\Sec4figs\marg1550-vs-ppb.png')

%%
```

```
98
   elec_pwr = 5.7; % NODE: 5.7 W -> 200 mW laser power
100 range = 200000; % FLARE: 200 km

102 shg_eff = 0.65:0.01:0.85;

104 pt_1550 = elec_pwr.*edfa_eff.*10^(Ltx/10);
   pt_775 = (elec_pwr - shg_pwr).*edfa_eff.*shg_eff.*10^(Ltx/10);
106
   [~,~,~,~,marg_1550,~,~] = base_1550(pt_1550,theta_1550,range,Lsky);
108 [~,~,~,~,marg_775,~,~] = base_775(pt_775,theta_775,range,Lsky);

110 marg_diff = marg_775 - marg_1550;

112 figure4 = figure;
   plot(shg_eff,marg_diff)
114 %set(gca,'xscale','log')
   xlabel('SHG conversion efficiency')
116 ylabel('Difference in link margin (dB)')

118 saveas(figure4,'C:\Users\Jimmy\Documents\MIT\Graduate Research\MS
      Thesis Template\Sec4figs\margdiff-vs-shg.png')
```

A.1.7 Case 3: Diffraction-limited, 2-cm aperture

```
%% Case 3: Diffraction-limited 2 cm aperture

close all;
%%
elec_pwr_vec = linspace(5,50); % Electrical power to transmitter,
    Watts
range_vec = logspace(5,7); % Range, 10^x meters

Ltx = -3; % For polarization-switching

Lsky = 0; % Space-to-space link, no atmospheric noise

shg_pwr = 0.62; % For a 3.3V polarization switcher at 50 ohm -> 0.22
     watts, plus 0.4 W for TEC.
edfa_eff = 0.035; % based on Ryan's thesis -- 200 mW optical from
    5.7 W electrical.
shg_eff = 0.75; % 0.75 based on experiment w/ Bill at JPL -- could
    be as much as 84% according to ThorLabs ads.

Dtx =  0.02;

lambda_1550 = 1.55e-6;
lambda_775 = 775e-9;

theta_1550 = 2*1.22*lambda_1550/Dtx;
theta_775 = 2*1.22*lambda_775/Dtx;

elec_pwr = 5.7; % NODE: 5.7 W -> 200 mW laser power
range = 200000; % FLARE: 200 km

pt_1550 = elec_pwr.*edfa_eff.*10^(Ltx/10);
pt_775 = (elec_pwr - shg_pwr).*edfa_eff.*shg_eff.*10^(Ltx/10);

[~,~,~,~,marg_1550,~,~] = base_1550(pt_1550,theta_1550,range,Lsky);
```

```
[~,appmag,~,~,marg_775,~,~] = base_775(pt_775,theta_775,range,Lsky);

marg_diff = marg_775 - marg_1550;

display(marg_diff)
display(appmag)

%%
[elec_pwr,range] = ndgrid(elec_pwr_vec,range_vec);

pt_1550 = elec_pwr.*edfa_eff.*10^(Ltx/10);
pt_775 = (elec_pwr - shg_pwr).*edfa_eff.*shg_eff.*10^(Ltx/10);

[~,~,~,~,marg_1550,~,~] = base_1550(pt_1550,theta_1550,range,Lsky);
[~,~,~,~,marg_775,~,~] = base_775(pt_775,theta_775,range,Lsky);
marg_diff = marg_775 - marg_1550;

%%

figure1 = figure;

contour(range./1000,elec_pwr,marg_diff,'ShowText','on');
xlabel('Range (km)')
ylabel('Electrical power to transmitter (W)')
set(gca,'xscale','log')

saveas(figure1,'C:\Users\Jimmy\Documents\MIT\Graduate Research\MS
    Thesis Template\Sec4figs\link-budget-improvement-2cmdiff.png')

%%

elec_pwr = 5.7;
range = logspace(5,7);

pt_1550 = elec_pwr.*edfa_eff.*10^(Ltx/10);
pt_775 = (elec_pwr - shg_pwr).*edfa_eff.*shg_eff.*10^(Ltx/10);
```

```
66
   [Prx_1550,~,~,Mopt_1550,marg_1550,~,sigma2_on_1550] = base_1550(
      pt_1550,theta_1550,range,Lsky);
68 [Prx_775,~,~,Mopt_775,marg_775,~,sigma2_on_775] = base_775(pt_775,
      theta_775,range,Lsky);
   marg_diff = marg_775 - marg_1550;
70
   Prx_1550_db = 10.*log10(Prx_1550);
72 Prx_775_db = 10.*log10(Prx_775);

74 %%

76 figure2 = figure;
   plot(range./1000,Mopt_1550)
78 set(gca,'xscale','log')
   xlabel('Range (km)')
80 ylabel('Optimum InGaAs (1550 nm) gain')

82 figure3 = figure;
   plot(range./1000,Mopt_775)
84 set(gca,'xscale','log')
   xlabel('Range (km)')
86 ylabel('Optimum Silicon (775 nm) gain')

88 figure4 = figure;
   plot(range./1000,sigma2_on_1550,range./1000,sigma2_on_775)
90 set(gca,'xscale','log')
   legend('1550','775');
92 xlabel('Range (km)')
   ylabel('\sigma^2 of photocurrent of on-pulse (A^2)')
94
   figure5 = figure;
96 plot(Prx_1550_db,Mopt_1550)
   xlabel('Received power (dB)')
98 ylabel('Optimum APD gain')
```

```
figure6 = figure;
plot(Prx_775_db,Mopt_775)
xlabel('Received power (dB)')
ylabel('Optimum APD gain')

figure7 = figure;
plot(Prx_1550_db,Mopt_1550,Prx_775_db,Mopt_775)
legend('1550','775')
xlabel('Received power (dB)')
ylabel('Optimum APD gain')

figure8 = figure;
plot(range./1000,Mopt_1550,range./1000,Mopt_775)
legend('1550','775')
set(gca,'xscale','log')
%set(gca,'yscale','log')
xlabel('Range (km)')
ylabel('Optimum APD gain')

saveas(figure2,'C:\Users\Jimmy\Documents\MIT\Graduate Research\MS
    Thesis Template\Sec4figs\optimum-ingaas-gain-2cmdiff.png')
saveas(figure3,'C:\Users\Jimmy\Documents\MIT\Graduate Research\MS
    Thesis Template\Sec4figs\optimum-silicon-gain-2cmdiff.png')
saveas(figure4,'C:\Users\Jimmy\Documents\MIT\Graduate Research\MS
    Thesis Template\Sec4figs\sigma2on-2cmdiff.png')
saveas(figure5,'C:\Users\Jimmy\Documents\MIT\Graduate Research\MS
    Thesis Template\Sec3figs\optimum-gain-ingaas.png')
saveas(figure6,'C:\Users\Jimmy\Documents\MIT\Graduate Research\MS
    Thesis Template\Sec3figs\optimum-gain-silicon.png')
saveas(figure7,'C:\Users\Jimmy\Documents\MIT\Graduate Research\MS
    Thesis Template\Sec3figs\optimum-gain-apd.png')
saveas(figure8,'C:\Users\Jimmy\Documents\MIT\Graduate Research\MS
    Thesis Template\Sec4figs\optimum-apd-gain-2cmdiff.png')
```

A.1.8 Case 4: High-cost SHG FLARE

```
%% Case 4: High-SHG-cost FLARE
close all;
%%
elec_pwr_vec = linspace(5,50); % Electrical power to transmitter,
    Watts
range_vec = logspace(5,7); % Range, 10^x meters



Ltx = 0; % Using thermal-switching

Lsky = 0; % Space-to-space link, no atmospheric noise

shg_pwr = 3.5; % Assuming direct oven "transplant"

edfa_eff = 0.035; % based on Ryan's thesis -- 200 mW optical from
    5.7 W electrical.

shg_eff = 0.75; % 0.75 based on experiment w/ Bill at JPL -- could
    be as much as 84% according to ThorLabs ads.

BW = 2.26e-3;

elec_pwr = 5.7; % NODE: 5.7 W -> 200 mW laser power
range = 200000; % FLARE: 200 km

pt_1550 = elec_pwr.*edfa_eff.*10^(Ltx/10);
pt_775 = (elec_pwr - shg_pwr).*edfa_eff.*shg_eff.*10^(Ltx/10);

[~,~,~,~,marg_1550,~,~] = base_1550(pt_1550,BW,range,Lsky);
[~,appmag,~,~,marg_775,~,~] = base_775(pt_775,BW,range,Lsky);

marg_diff = marg_775 - marg_1550;

```

```
display(marg_diff)
display(appmag)

%%
[elec_pwr,range] = ndgrid(elec_pwr_vec,range_vec);

pt_1550 = elec_pwr.*edfa_eff.*10^(Ltx/10);
pt_775 = (elec_pwr - shg_pwr).*edfa_eff.*shg_eff.*10^(Ltx/10);

[~,~,~,~,marg_1550,~,~] = base_1550(pt_1550,BW,range,Lsky);
[~,~,~,~,marg_775,~,~] = base_775(pt_775,BW,range,Lsky);
marg_diff = marg_775 - marg_1550;

%%

figure1 = figure;

contour(range./1000,elec_pwr,marg_diff,'ShowText','on');
xlabel('Range (km)')
ylabel('Electrical power to transmitter (W)')
set(gca,'xscale','log')

saveas(figure1,'C:\Users\Jimmy\Documents\MIT\Graduate Research\MS
    Thesis Template\Sec4figs\link-budget-improvement-highcost.png')
```

A.1.9 Case 5: Half-beamwidth FLARE

```
%% Case 5: Half-beamwidth FLARE
close all;
%%
elec_pwr_vec = linspace(5,50); % Electrical power to transmitter,
    Watts
range_vec = logspace(5,7); % Range, 10^x meters



Ltx = 0; % No SHG at all, no polarization switching

Lsky = 0; % Space-to-space link, no atmospheric noise

edfa_eff = 0.035; % based on Ryan's thesis -- 200 mW optical from
    5.7 W electrical.

BW_1 = 2.26e-3;
BW_2 = BW_1/2;  %

elec_pwr = 5.7; % NODE: 5.7 W -> 200 mW laser power
range = 200000; % FLARE: 200 km

pt_1550 = elec_pwr.*edfa_eff.*10^(Ltx/10);

[~,~,~,~,marg_1,~,~] = base_1550(pt_1550,BW_1,range,Lsky);
[~,~,~,~,marg_2,~,~] = base_1550(pt_1550,BW_2,range,Lsky);

marg_diff = marg_2 - marg_1;

display(marg_diff)

%%
[elec_pwr,range] = ndgrid(elec_pwr_vec,range_vec);

```

```
pt_1550 = elec_pwr.*edfa_eff.*10^(Ltx/10);

[~,~,~,~,marg_1,~,~] = base_1550(pt_1550,BW_1,range,Lsky);
[~,~,~,~,marg_2,~,~] = base_1550(pt_1550,BW_2,range,Lsky);
marg_diff = marg_2 - marg_1;

%%

figure1 = figure;

contour(range./1000,elec_pwr,marg_diff,'ShowText','on.');
xlabel('Range (km)')
ylabel('Electrical power to transmitter (W)')
set(gca,'xscale','log')

saveas(figure1,'C:\Users\Jimmy\Documents\MIT\Graduate Research\MS
    Thesis Template\Sec4figs\link-budget-improvement-halfBW.png')

%%

elec_pwr = 5.7;
range = logspace(5,7);

pt_1550 = elec_pwr.*edfa_eff.*10^(Ltx/10);

[~,~,~,Mopt_1,marg_1,~,sigma2_on_1] = base_1550(pt_1550,BW_1,range,
    Lsky);
[~,~,~,Mopt_2,marg_2,~,sigma2_on_2] = base_1550(pt_1550,BW_2,range,
    Lsky);
marg_diff = marg_2 - marg_1;

%%

figure2 = figure;
plot(range./1000,Mopt_1,range./1000,Mopt_2)
legend('2.26 mrad','1.13 mrad')
```

```
set(gca,'xscale','log')
xlabel('Range (km)')
ylabel('Optimum gain')

figure3 = figure;
plot(range./1000,sigma2_on_1,range./1000,sigma2_on_2)
set(gca,'xscale','log')
legend('2.26 mrad','1.13 mrad')
xlabel('Range (km)')
ylabel('\sigma^2 of photocurrent of on-pulse (A^2)')
```

A.2 Geiger-mode Channel Capacity

The chancap function calculates the capacity of an optical link via Equation 2.1. It receives signal and noise power from gmapd (via Equation 1.10), which is wrapped by basegmapd and then basegmapd1550 and basegmapd775, as was done for the linear-mode regime. Finally, basegmapd1550 and basegmapd775 are called by case6_flare_gmapd to generate the plots.

A.2.1 chancap

```
function [ cap ] = chancap( lambda, Pr, Pn, PPM, Ts)
%CHANCAP Capacity of a PPM channel.
%   Inputs: wavelength (meters), received and noise power, PPM order
    , slot width.

c = 299792458;
h = 6.626e-34;
E = h*c./lambda;

cap = (1./(E.*log(2))).*(Pr.^2./(Pr./log(PPM) + 2.*Pn./(PPM-1) + Pr
    .^2.*PPM.*Ts./(E.*log(PPM)) ));

end
```

A.2.2 gmapd

```
function [snr,cap,ppb] = gmapd(lambda,Ptx,PPM,Ts,range,Drx,BW,Lrx,
    PDE,lam_d,n_pix,p_aft)

c = 299792458; % speed of light
h = 6.626e-34; % Planck
E = h*c./lambda;

spaceloss = (lambda./(4.*pi.*range)).^2;

Grx = (pi.*Drx./lambda).^2;

Gtx = 2/(1 - cos(BW./2));

Prx = Ptx.*Gtx.*spaceloss.*Grx.*10.^(Lrx./10);

lam_p = Prx.*Ts./(E.*n_pix); % Photons per gate = (W/sec) * (slot
    time) /( E/photon * number of APD pixels)

snr = snrgmapd(PDE, lam_p, lam_d, n_pix, p_aft);

cap = chancap(lambda, Prx, Prx./snr, PPM, Ts);

ppb = Prx./(E.*cap);

end
```

A.2.3 basegmapd

```
function [snr,cap,ppb] = basegmapd(lambda,Ptx,range,BW,PDE,lam_d,
    n_pix,p_aft)

Ts = 40e-9; % Pulsewidth of Hamamatsu GM-APD is 20 ns, so the slot
    width should be 2x that.
Drx = 0.085; % 85 mm aperture, from FLARE proposal
PPM = 64; % Per Kingsbury/NODE
Lrx = 0; % Assume no optical loss in the detector.

[snr,cap,ppb] = gmapd(lambda,Ptx,PPM,Ts,range,Drx,BW,Lrx,PDE,lam_d,
    n_pix,p_aft);

end
```

A.2.4 basegmapd1550

```
function [snr,cap,ppb] = basegmapd1550(Ptx,range,BW)

lambda = 1550e-9;
PDE = 0.27;% Per Boeing/Spectralab, 9002-10, 300 K, fig 5
lam_d = 25*40e-9; %25 KHz (i.e. counts-per-second) estimated from
    figure, divided by 1024 cells, times slotwidth.
n_gates = 1024; % 32x32 array
p_aft = 0.001;% Not given in reference -- baselining the same as
    Hamamatsu's Si

[snr,cap,ppb] = basegmapd(lambda,Ptx,range,BW,PDE,lam_d,n_gates,
    p_aft);

end
```

A.2.5 basegmapd775

```
function [snr,cap,ppb] = basegmapd775(Ptx,range,BW)

lambda = 775e-9;
PDE = 0.40; % Per Hamamatsu, model C13366-1350GD
lam_d = 3.75*40e-9; % 2.5 kcps overall, divided by 667 cells, times
    slotwidth.
n_gates = 667;
p_aft = 0.001;

[snr,cap,ppb] = basegmapd(lambda,Ptx,range,BW,PDE,lam_d,n_gates,
    p_aft);

end
```

A.2.6 Case 6: Diffraction-limited FLARE with GM-APD

```
%% Case 1: FLARE

close all;

elec_pwr_vec = linspace(5,50); % Electrical power to transmitter,
    Watts
range_vec = logspace(5,7); % Range, 10^x meters




Ltx = -3; % For polarization-switching

shg_pwr = 0.62; % For a 3.3V polarization switcher at 50 ohm -> 0.22
     watts, plus 0.4 W for TEC.

edfa_eff = 0.035; % based on Ryan's thesis -- 200 mW optical from
    5.7 W electrical.

```

```
shg_eff = 0.75; % 0.75 based on experiment w/ Bill at JPL -- could
    be as much as 84% according to ThorLabs ads.

lambda_1550 = 1.55e-6;
lambda_775 = 775e-9;

Dtx =  0.00167345; %Equivalent to get the same BW as NODE in a
    diffraction-limited system

theta_1550 = 2*1.22*lambda_1550/Dtx;
theta_775 = 2*1.22*lambda_775/Dtx;

elec_pwr = 5.7; % NODE: 5.7 W -> 200 mW laser power
range = 200000; % FLARE: 200 km

pt_1550 = elec_pwr.*edfa_eff.*10^(Ltx/10);
pt_775 = (elec_pwr - shg_pwr).*edfa_eff.*shg_eff.*10^(Ltx/10);

[snr_1550,cap_1550,ppb_1550] = basegmapd1550(pt_1550,range,
    theta_1550);
[snr_775,cap_775,ppb_775] = basegmapd775(pt_775,range,theta_775);


cap_fact = cap_775./cap_1550;

cap_fact = 10*log10(cap_fact);

display(cap_fact)

%%

elec_pwr = 5.7;
range = logspace(5,9);

pt_1550 = elec_pwr.*edfa_eff.*10^(Ltx/10);
pt_775 = (elec_pwr - shg_pwr).*edfa_eff.*shg_eff.*10^(Ltx/10);
```

```
49
   [snr_1550,cap_1550,ppb_1550] = basegmapd1550(pt_1550,range,
      theta_1550);
51 [snr_775,cap_775,ppb_775] = basegmapd775(pt_775,range,theta_775);

53 cap_1550_db = 10*log10(cap_1550);
   cap_775_db = 10*log10(cap_775);
55
   %%
57
   figure1 = figure;
59 plot(range./1000,cap_775_db-cap_1550_db)
   set(gca,'xscale','log')
61 xlabel('Range (km)')
   ylabel('Improvement in channel capacity (dB)')
63
   figure2 = figure;
65 plot(range./1000,cap_1550,range./1000,cap_775)
   legend('1550','775')
67 set(gca,'xscale','log')
   set(gca,'yscale','log')
69 xlabel('Range (km)')
   ylabel('Channel capacity (bps)')
71
   figure3 = figure;
73 plot(range./1000,snr_1550_db,range./1000,snr_775_db)
   legend('1550','775')
75 set(gca,'xscale','log')
   xlabel('Range (km)')
77 ylabel('SNR (dB)')

79 figure4 = figure;
   plot(ppb_1550,cap_1550,ppb_775,cap_775)
81 legend('1550','775','Location','southwest')
   set(gca,'xscale','log')
83 set(gca,'yscale','log')
```

```
xlabel('Photons per bit')
ylabel('Data rates (bps)')

saveas(figure2,'C:\Users\Jimmy\Documents\MIT\Graduate Research\MS
    Thesis Template\Sec4figs\chancap-flarediff-gmapd.png')
saveas(figure3,'C:\Users\Jimmy\Documents\MIT\Graduate Research\MS
    Thesis Template\Sec4figs\snr-flarediff-gmapd.png')
```

Bibliography

[1] Thorlabs, "Periodically Poled Lithium Niobate (PPLN) - Tutorial," Tech. rep., n.d.

[2] Kerri Cahoy, "FLARE: Free-space Lasercom and Radiation Experiment," 2015.

[3] Hamamatsu, "Characteristics and use of Si APD (Avalanche Photodiode)," Tech. Rep. SD-28, n.d.

[4] Federal Communications Commission, "FCC Form 605," .

[5] Federal Aviation Administration, "Order JO 7400.2K: Procedures for Handling Airspace Matters," 2014.

[6] Bruce Moision and William Farr, "Range Dependence of the Optical Communications Channel," Tech. Rep. 42-199B, Nov. 2014.

[7] Boroson, D. M., Robinson, B. S., Murphy, D. V., Burianek, D. A., Khatri, F., Kovalik, J. M., Sodnik, Z., and Cornwell, D. M., "Overview and results of the Lunar Laser Communication Demonstration," Vol. 8971, 2014, pp. 89710S–89710S–11.

[8] Ryan Kingsbury, *Optical Communications for Small Satellites*, Ph.D. thesis, Massachusetts Institute of Technology, Aug. 2015.

[9] BridgeSat Inc., "Products - Satellite data collection, bandwidth, ground network services," n.d.

[10] Elizabeth Buchen and Dominic DePasquale, "2014 Nano / Microsatellite Market Assessment," 2014.

[11] The Tauri Group, "2015 State of the Satellite Industry Report," Sept. 2015.

[12] "Power | KitCube," 2015.

[13] Bahaa E. A. Saleh and Malvin Carl Teich, "Nonlinear Optics," *Fundamentals of Photonics*, Wiley, 2nd ed., 2007, pp. 875–917.

[14] Bahaa E. A. Saleh and Malvin Carl Teich, "Electromagnetic Optics," *Fundamentals of Photonics*, Wiley, 1st ed., 1991, pp. 157–192.

[15] Rüdiger Paschotta, "Frequency Doubling," n.d.

[16] Hamamatsu, "InGaAs Photodiodes Selection Guide," March 2015.

[17] Hamamatsu, "Si APD (Avalanche Photodiode) Selection Guide," March 2014.

[18] Excelitas Technologies, "Avalanche photodiode: A User Guide," Tech. rep., n.d.

[19] Govind P. Agrawal, "Optical Communication Systems (OPT428)," n.d.

[20] Robinson, B. S., Caplan, D. O., Stevens, M. L., Barron, R. J., Dauler, E. A., and Hamilton, S. A., "1.5-photons/bit photon-counting optical communications using Geiger-mode avalanche photodiodes," *2005 Digest of the LEOS Summer Topicals*, 2003.

[21] Kolb, K., "Signal-to-noise ratio of Geiger-mode avalanche photodiode single-photon counting detectors," *Optical Engineering*, Vol. 53, No. 8, 2014, pp. 081904–081904.

[22] Hamamatsu, "MPPC®and MPPC®module for precision measurement," March 2016.

[23] Yuan, P., Boisvert, J., Sudharsanan, R., Isshiki, T., McDonald, P., Salisbury, M., Liu, M., and Campbell, J. C., "High efficiency 1.55 μm Geiger-mode single photon counting avalanche photodiodes operating near 0 C," *Integrated Optoelectronic Devices 2008*, International Society for Optics and Photonics, 2008, pp. 69001B–69001B.

[24] Hemmati, H., editor, *Near-Earth Laser Communications*, Vol. 20094921 of *Optical Science and Engineering*, CRC Press, March 2009.

[25] Alexander, S. B., *Optical Communication Receiver Design*, SPIE, 1000 20th Street, Bellingham, WA 98227-0010 USA, Jan. 1997.

[26] Bruce Moision and Hua Xie, "An Approximate Link Equation for the Direct-Detected Optical PPM Link," Tech. Rep. 42-199A, Nov. 2014.

[27] Emily Clements, "Notes on NODE Link Budget Analysis with Uncertainty and Sensitivity Analysis," manuscript submitted.

[28] Princeton Instruments Imaging Group, "Introduction to scientific InGaAs FPA camera," n.d.

[29] Fields, R., Kozlowski, D., Yura, H., Wong, R., Wicker, J., Lunde, C., Gregory, M., Wandernoth, B., and Heine, F., "5.625 Gbps bidirectional laser communications measurements between the NFIRE satellite and an Optical Ground Station," *2011 International Conference on Space Optical Systems and Applications (ICSOS)*, May 2011, pp. 44–53.

[30] Heine, F., Kämpfner, H., Czichy, R., Meyer, R., and Lutzer, M., "Optical inter-satellite communication operational," *MILITARY COMMUNICATIONS CONFERENCE, 2010 - MILCOM 2010*, Oct. 2010, pp. 1583–1587.

[31] Janson, S. and Welle, R., "The NASA Optical Communication and Sensor Demonstration Program," *AIAA/USU Conference on Small Satellites*, Aug. 2013.

[32] Darren Rowen, Rick Dolphus, Patrick Doyle, and Addison Faler, "OCSD-A / AeroCube 7-A Status Update," *Cal Poly CubeSat Developer's Workshop*, 2016.

[33] "KitCube | Taking CubeSats farther than ever before," 2015.

[34] Covesion, "PV Oven Series," 2015.

[35] Cheng, C., Chandrasekara, R., Tan, Y. C., and Ling, A., "Space qualified nanosatellite electronics platform for photon pair experiments," *arXiv:1505.06523 [physics, physics:quant-ph]*, May 2015, arXiv: 1505.06523.

[36] Bedington, R., Truong-Cao, E., Chuan, T. Y., Cheng, C., Durak, K., Grieve, J. A., Larsen, J., Oi, D., and Ling, A., "Deploying quantum light sources on nanosatellites II: lessons and perspectives on CubeSat spacecraft," *arXiv:1508.07074 [physics, physics:quant-ph]*, Oct. 2015, pp. 964811, arXiv: 1508.07074.

[37] Schweitzer, S., Kirchengast, G., and Proschek, V., "Atmospheric influences on infrared-laser signals used for occultation measurements between Low Earth Orbit satellites," *Atmos. Meas. Tech.*, Vol. 4, No. 10, Oct. 2011, pp. 2273–2292.

[38] Albert, J., "Satellite-mounted Light Sources as Photometric Calibration Standards for Ground-based Telescopes," *The Astronomical Journal*, Vol. 143, No. 1, 2012, pp. 8.

[39] Versawave, "40 Gb/s 3.3V Polarization Modulator," n.d.

[40] Oaida, B. V., Wu, W., Erkmen, B. I., Biswas, A., Andrews, K. S., Kokorowski, M., and Wilkerson, M., "Optical link design and validation testing of the Optical Payload for Lasercomm Science (OPALS) system," Vol. 8971, 2014, pp. 89710U–89710U–15.

[41] The Aerospace Corporation, "2015 Annual Report," 2015.

[42] Steve Blair, "ECE 5411 - Optical Communcation Systems: Receiver noise," March 2012.

[43] Ou, Z. Y., Pereira, S. F., Polzik, E. S., and Kimble, H. J., "85% efficiency for cw frequency doubling from 1.08 to 0.54 μm," *Optics Letters*, Vol. 17, No. 9, May 1992, pp. 640.

[44] Bosenberg, W. R., Pelouch, W. S., and Tang, C. L., "High-efficiency and narrow-linewidth operation of a two-crystal β-BaB2O4 optical parametric oscillator," *Applied Physics Letters*, Vol. 55, No. 19, Nov. 1989, pp. 1952–1954.

[45] Coherent Inc., "Mira-OPOX, an optical parametric oscillator (OPO)," n.d.

[46] Andreas Fix, Christian Büdenbender, Martin Wirth, Mathieu Quatrevalet, Axel Amediek, Christoph Kiemle, and Gerhard Ehret, "Optical parametric oscillators and amplifiers for airborne and spaceborne active remote sensing of CO2 and CH4," *SPIE Remote Sensing*, International Society for Optics and Photonics, 2011, pp. 818206–818206.